This is to certify that the

dissertation entitled

"Irreversibility and Vortex Pinning in Nb/CuX Multilayers"

presented by

Carl Norman Hoff

has been accepted towards fulfillment
of the requirements for

Ph.D. degree in Physics

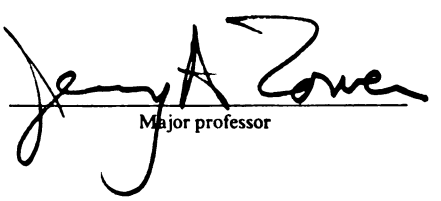

Major professor

Date December 16, 1996

Irreversibility and Vortex Pinning in Nb/CuX Multilayers

By

Carl Norman Hoff

A DISSERTATION

Submitted to
Michigan State University
in partial fulfillment of the requirements
for the degree of

DOCTOR OF PHILOSOPHY

Department of Physics and Astronomy

1996

Ir

susce

Cu,

susce

Meas

have

700 Å

believ

data h

consis

also b

sputter

either

perpen

ABSTRACT

Irreversibility and Vortex Pinning in Nb/CuX Multilayers

By

Carl Norman Hoff

The irreversibility between the zero field cooled (ZFC) and field cooled (FC) susceptibilities of sputtered Nb/CuX multilayers has been measured. CuX is either pure Cu, CuGe(2%), CuGe(5%) or CuMn(0.3%). The temperature T_{irr} below which the susceptibility is irreversible is measured as a function of field perpendicular to the layers. Measurements with the field parallel to the layers had irreproducible results. All samples have Nb layers 280Å thick with the normal metal layer thickness d_N between 20Å and 700Å with T_{irr} measured in fields from 25G to 3000G. The curve $T_{irr}(H)$ or $H_{irr}(T)$ is believed to be the phase boundary between the vortex solid and the vortex liquid. The data has been fit to the form $H_{irr}(T) = H_{irr_0}(1 - T/T_{c_0})^P$ and values of P are found that are consistent with theory. The critical current density J_c and pinning force density F_p have also been measured in patterned Nb/CuX multilayers. These samples were fabricated by sputtering through a trilayer photolithographic mask. In these measurements CuX is either pure Cu, CuGe(2%), CuGe(10%) or CuMn(0.3%). Measurements with the field perpendicular and parallel to the layers were performed, both with the current in the plane

of the multilayers and perpendicular to the field. Again all samples have Nb layers 280Å thick but the normal metal layer thickness d_N was varied between 25Å and 100Å. In the perpendicular orientation evidence of a transition from 3D line to 2D pancake vortices was found in the pinning force density data. In the parallel orientation it is demonstrated that the pinning strength of the N layers is affected by the addition of Ge, with no detrimental effects on T_c. Study of these superconducting/normal metal multilayers proves to be a good approach to understanding similar process in high-T_c superconductors which have limited the useful devices that can be made from these materials.

to my parents

and su

encour

sputter

early ir

Jim Mu

the shop

help wit

MSU wi

support f

and thank

encourag

providing

Fi

Physics ar

Science Fo

ACKNOWLEDGMENTS

Many thanks go to my thesis advisor, Professor Jerry A. Cowen for his guidance and support for the duration of this project. I am especially grateful for his patience and encouragement during the writing and editing of this dissertation.

A special thanks goes to Reza Loloee for his help with the "Squids" and the sputtering system. Thanks are due Mike Wilson for the use of some of his samples in the early irreversibility measurements. Thanks are also due the shop guys, Tom Palazzolo, Jim Muns, and Tom Hudson for the many times they rushed one of my projects through the shop with sometimes very short notice. A special thanks goes to Carol Flegler for her help with the EDS studies. I'd also like to thank all the graduate students and staff at MSU who helped me maintain my sanity over the past five and a half years.

My parents, J. M. and Onalee Hoff, deserve special recognition since without their support for the last 28 years, I could never have made it this far. My greatest appreciation and thanks must extend to my wife Patricia and my son Scott. I thank my wife for all her encouragement, support, and love these past few years. I thank my son for always providing a necessary diversion, and for reminding me of the really important things in life.

Financial support for this project was generously provided by the Department of Physics and Astronomy, the Center of Fundamental Materials Research, and the National Science Foundation.

TABLE OF CONTENTS

CH
CR

CHA
FUTU

LIST

LIST OF TABLES

LIST OF FIGURES

Figure 3

Figure 3

Figure 3

Figure 3

Figure 3

Figure 3

Figure 3

Figure 3

Figure 3

Figure 3

Figure 3

Figure 3

Figure 3

Figure 3

Figure 3

Figure 3

Figure 3

Figure 3

Figure 4

Figure 4

Figure 5

Figure 5

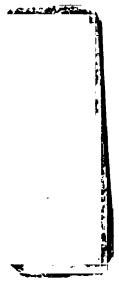

the c

are t

unde

relat

Whe

move

drivi

steac

appe

dissi

the u

desir

drivi

affect

densit

Chapter 1

INTRODUCTION

The properties of anisotropic superconductors are particularly important in light of the discovery of high-T_c superconductivity in anisotropic metallic oxides. Though these are the best known anisotropic superconductors, they are the least understood. The understanding of the physical properties of these high-T_c compounds is limited by the relatively small size of parameter space that is explorable.

In all type-II superconductors, a vortex system is formed above the Meissner state. When an external current density j is applied to the vortex system, the flux lines start to move under the action of the Lorentz force. Within a perfect homogeneous system the driving Lorentz force is counteracted only by a frictional force proportional to the steady-state velocity of the vortex system. The consequence of this flux motion is the appearance of a finite electric field and dissipation. The desired property of dissipation-free current flow is then lost. It is precisely this problem that severely limits the usefulness of high-T_c superconductors in practical applications. In order to recover the desired dissipation-free current flow, the flux lines have to be pinned. In this case the driving Lorentz force is counteracted by a pinning force. Fortunately, any static disorder affecting the superconducting order parameter will contribute to a finite pinning force density, thereby reestablishing the technological usefulness of type-II superconductors.

However, the issue of dissipation-free current flow has now become a matter of optimizing the pinning force density, since increasing the current density until the Lorentz force overcomes the pinning force causes dissipation to reappear as the vortices become depinned.

Much work[1] both theoretical and experimental has been done on vortices in high-T_c superconductors, but there is still much that is not well understood. This study focuses on low-T_c superconductor / normal metal multilayers which show many of the same properties as the high-T_c superconductor but the range of explorable parameter space is much larger. All samples in this study are Nb/CuX multilayers, where CuX is either pure copper, CuGe, or CuMn. Ge is a nonmagnetic impurity which doesn't break Cooper pairs, and Mn is a magnetic impurity which does break Cooper pairs. Unlike the study of high-T_c compounds where the number of variable parameters is very limited, here the thickness of the superconducting layer d_S, the normal metal layer thickness d_N, and the concentration and type of impurity in the normal metal layer can all be varied. Figure 1 illustrates all these variable parameters.

This study focuses on the investigation of two properties common to all type-II superconductors, the irreversibility line seen in magnetization measurements, and the critical current density. The irreversibility line, which is proposed to arise from the melting of a vortex solid to a vortex liquid, is of great interest to the study of dissipation-free current flow as only the vortex solid phase can be effectively pinned as the motion present in the liquid phase leads to dissipation. The critical current density is important as it allows one to calculate the pinning force density directly.

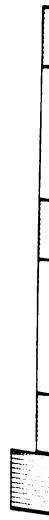

Figur

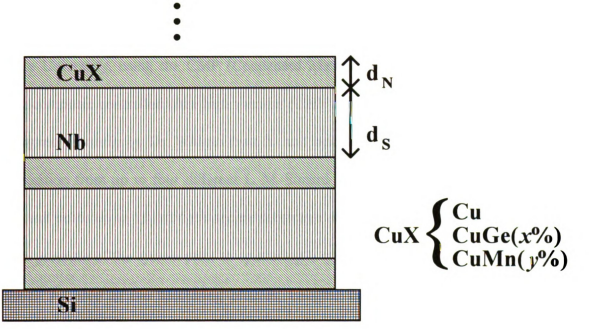

Figure 1 - A typical Nb/CuX multilayer which is produced by sputtering on a Si substrate. The normal metal layer thickness d_N was varied from 25Å to 700Å and the superconducting layer thickness was fixed at 280Å for this study. Typical in-plane dimensions are of the order of 1cm.

State

The c

desig

depos

run a

base p

purity

backgr

used i

substrat

process (

sputtering

Chapter 2

SAMPLE PREPARATION AND FABRICATION

The films and multilayered samples used in this study were fabricated at Michigan State University, using the CMP (Condensed Matter Physics group) sputtering system. The computer controlled ultra high vacuum (UHV) DC magnetron sputtering system was designed primarily by Dr. William Pratt Jr. and built by Simard Inc.[2] The system allows deposition from up to four different L. M. Simard "Tri-Mag" sputtering guns in a single run and holds up to 16 half-inch-square substrates or 32 smaller patterned substrates. The base pressure of the system prior to sputtering is typically $\leq 2.0\times10^{-8}$ torr. The ultra high purity Ar used in the sputtering process, coupled with the low base pressure, limits background contamination of the gas in the chamber to less than 10 ppm. All samples used in this study were deposited onto polished, single-crystal, (001)-oriented Si substrates.

The remainder of this section will detail substrate preparation, the patterning process (used for critical current measurements only), mounting of the samples in the sputtering system, and preparation and general aspects of the sputtering system.

2.1

used

squar

each

dehyd

are b

mour

cut it

hexar

5% N

at 90

hour a

milky

heating

with de

substrate

dehydrate

are blown

2.1 Substrates

All substrates are polished, single-crystal, (001)-oriented Si. For samples to be used in magnetization measurements, 3 inch diameter wafers[3] are cleaved into half inch squares. The square substrates are then sequentially washed ultrasonically for 5 minutes each in the following: alconox and deionized water, deionized water, acetone, and dehydrated ethyl alcohol. As soon as the substrates are removed from the alcohol, they are blown dry with compressed nitrogen and mounted in the sputtering system.

For samples to be used in the critical current measurements, a 3 inch wafer is mounted with paraffin in a surface grinder. A diamond impregnated wheel is then used to cut it into 0.16 inch by 0.25 inch rectangles. These substrates are washed ultrasonically in hexanes for 1 hour to remove any remaining paraffin, and then cleaned ultrasonically in a 5% MICRO[4] solution for 5 minutes. While still in the solution, they are heated for 1 hour at 90°C, cleaned in the ultrasonic bath for 5 more minutes, and heated for an additional hour at 90°C. By the end of the cleaning process, the 5% MICRO solution turns from a milky color to water clear. If any color remains after 1 hour into the final heating, the heating continues until all color is gone. The substrates are rinsed 5 times ultrasonically with deionized water for 5 minutes each time to remove all the cleaning solution. The substrates are then sequentially washed ultrasonically for 5 minutes each in acetone, and dehydrated ethyl alcohol. As soon as the substrates are removed from the alcohol, they are blown dry with compressed nitrogen.

2.2 Patterning (for Critical Current Measurements)

Before the fabrication of a lithographic mask on the substrates can be completed, one needs a contact film mask. It is called a contact mask, because the film is placed in direct contact with the spun photoresist when the pattern is transferred. Therefore the transferred pattern has dimensions essentially identical to the film pattern. The first step in creating the contact film mask, is generating the black and white pattern using a computer drawing package. The second step is printing the pattern on high quality paper, using a good laser printer to assure a high contrast image. Figure 2 shows the pattern used in these experiments. The third step is photographing the image, to transfer the pattern to film. For this step a Nikon FM2 camera is loaded with Kodak T-Max ISO 100 Professional B&W film.[5] Several pictures are taken with different parameters to assure that a good film mask will result. The film is developed using standard dark room

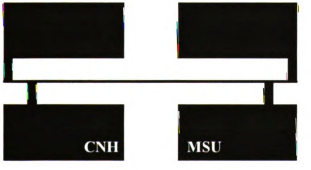

Figure 2 - The pattern (actual size) that was photographed to create the contact film mask. The actual photolithographic pattern is reduced by a factor of 15.4.

procedures and allowed to dry before it is inspected under a microscope to find the best film mask. For this experiment, the best mask was produced using a F-stop of 5.6 with a shutter time of 1/4 second.

A clean rectangular substrate is now ready for fabrication of the trilayer mask that will be used to create the patterned sample as illustrated in Figure 3. There are 10 steps in the creation of the mask. They are:

1. Spin on 1813 photoresist[6] at 4000 rpm for 30 seconds. This creates a uniform layer approximately 1.4μm thick.
2. Bake the sample for 1 hour at 90°C. If the temperature goes above 104°C the photoresist becomes so hard that it cannot be easily removed with acetone and therefore may not be used.
3. Expose the whole photoresist layer with an ultra-violet (UV) lamp for 8 seconds.
4. Evaporate a 340Å layer of Al at no more than 2 Å/second. The evaporator reaches a base pressure of 6×10^{-6} torr. The slow deposition rate is required to avoid excessively heating the photoresist and hardening the film. The thickness and deposition rate are monitored by a quartz crystal film thickness monitor.
5. Repeat step 1. This creates a second 1.4μm layer.
6. Repeat step 2.
7. Expose the photoresist layer covered with the desired 35mm film mask with a UV lamp for 9 seconds.
8. Place the sample in 452 developer[6] until the top layer of photoresist, the Al layer, and finally the photoresist beneath the Al layer is removed in the exposed areas. This step

takes about 2 minutes with new photoresist but can take up to 5 minutes with older photoresist. Photoresist older than 2 months should not be used. The progress of the developing can be checked under a microscope. If the developing is not complete (an undercut of about 2μm in the bottom photoresist layer should be seen) the sample may be placed back in the developer. Once developing is complete the sample is removed from the developer, rinsed in deionized water and blown dry with compressed N_2.

9. Repeat step 2. This bake is solely to help dry the samples and minimize outgassing when the samples are placed in the ultra high vacuum of the sputtering system.
10. Place the sample in a Plasma Therm[7] Batchtop System VII Reactive Ion Etcher (RIE). This etch is intended to remove any photoresist left on the Si substrates in the exposed areas. The system is pumped and purged several times until a base pressure of 13 mtorr or less is reached. Then a 20 watt oxygen etch is run for 30 seconds. The pressure set point is 50 mtorr and the oxygen flow rate is 7.5 sccm.

The samples are now ready to be mounted in the sputtering system. After the film or multilayer is deposited through the mask, the sample is removed from the sputtering system and the trilayer mask is removed by soaking the sample in acetone for a few minutes. See Figure 4 for an illustration of the final patterned sample.

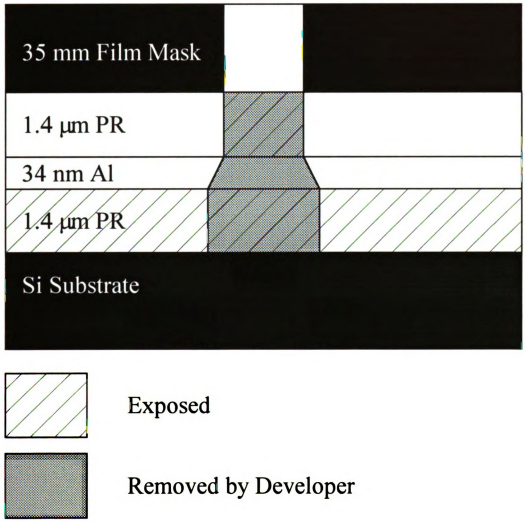

Figure 3 - The trilayer photoresist mask used to create the patterned samples.

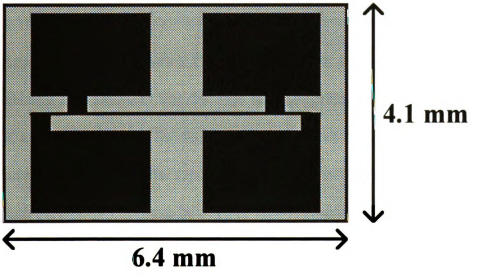

Figure 4 - An illustration of a patterned sample. The sample wire is 50μm wide and 5mm long while the contact pads are approximately 1mm by 2mm. The top two contact pads are for the voltage leads while the bottom two are for the current leads.

2.3 The Sputtering System

Both the square substrates and the patterned substrates are mounted in an aluminum holder as shown in Figure 5. The system can accommodate up to 8 substrate holders, each having 2 locations designed to hold a square substrate. A half inch square stainless steel support can be placed in each location to hold two of the patterned substrates. The holders are arranged on the SPAMA (Substrate Positioning And Masking Apparatus) plate as shown in Figure 6. Each holder employs one of two types of rotatable stainless steel shutters. The first type has one opening so that only one substrate location at a time can be used for deposition. The second type has two openings so that both substrate locations can be deposited on simultaneously. Both types of shutters also allow both substrate locations to be covered simultaneously to protect the substrates or already grown samples from unwanted deposition while a sample is being grown in another holder. The two holed shutters are good for making multiple samples with the same parameters. In addition to the substrate holders, the SPAMA plate also holds two quartz crystal film thickness monitors, one each for Nb and CuX.

The sputtering chamber is capable of reaching an ultimate base pressure of less than 2.0×10^{-8} torr. To achieve this pressure a high speed CTI Cryo Torr 8 cryopump is used to pump the system down, which takes roughly 2 days. The system is baked at 60°C during the first 10 to 12 hours of pumping. Once the base pressure is reached the partial pressures of the background gases inside the chamber are measured using a Dycor Electronics M100 Quadrapole Gas Analyzer. The gasses checked included He, H_2O, N_2,

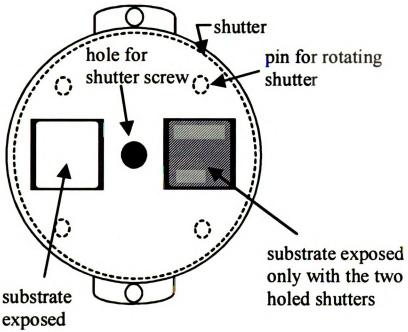

Figure 5 - Diagram of the substrate holders used in this study. The shutters could be rotated by pulling on one of the pins with an externally controlled wobble stick.

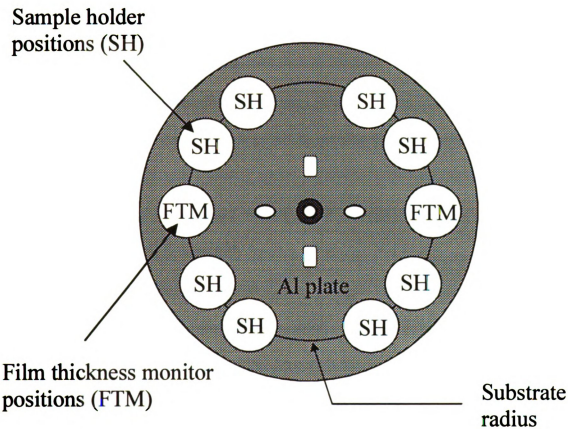

Figure 6 - Diagram of the Sample Positioning and Masking Apparatus (SPAMA) plate.

O_2, and Ar. The partial pressures of H_2O vapor and N_2 gas are always the highest with partial pressures between 10^{-8} and 10^{-9} torr. All other gases have partial pressures at least an order of magnitude lower.

The substrate temperature is stabilized during sample deposition by using a Cu block and foil to thermally link the substrate to the Al holder. Since the Cu blocks are pressed against the back of the substrates they also keep the substrates from moving as the SPAMA plate rotates. The Al holders are in turn thermally linked to an internal liquid N_2 reservoir located at the bottom of the shaft holding the SPAMA plate as shown in Figure 7. The internal reservoir is kept full by passing high pressure (1000 psi) N_2 gas through a fine stainless steel capillary cooled by an external heat exchanger. The heat exchanger consists of the capillary welded inside a length of 1/4 inch copper tubing, through which liquid N_2 is constantly flowing. The high pressure N_2 gas is then liquefied and continues through the fine stainless steel capillary to the internal reservoir. With this cooling system, heat that is deposited in the substrate by the incoming sputtered atoms is conducted away from the sample to the Al sample holder by the Cu foil. Heat is then progressively transferred to the SPAMA plate, to four OFHC (Oxygen Free High Conductivity) Cu rods, and finally to the internal liquid N_2 reservoir where evaporated N_2 gas carries the heat out of the system through a second stainless steel capillary. An important part of this design is the use of the small capillaries which permit the whole assembly of the internal reservoir and the SPAMA plate to rotate. The Cu tube carrying liquid N_2 in the external heat exchanger continues on to a large internal ring or Meissner trap around the top of the chamber before being vented to the outside. The Meissner trap

is used to freeze out impurities inside the chamber. A thermocouple placed on this ring is used to confirm that liquid N_2 is flowing. With the cooling system in place, thermocouples placed on top of the Cu blocks are used to monitor the temperature throughout the sputtering run. Since each thermocouple is separated from the actual deposition surface by the Cu block and the Si substrate, the samples certainly get hotter than the monitored temperatures. For the typical square substrates, the thermocouple temperatures are kept between -20°C and +20°C for the duration of a run. With the patterned substrates, these temperatures are kept between -60°C and -40°C. The reason for the lower temperatures for the patterned samples is two fold. First, it minimizes outgassing from the photoresist and second, it avoids excessive heating and hardening of the photoresist.

The sputtering system contained four different L. M. Simard "Tri-Mag" or triode, magnetron sputtering guns. A schematic of one gun is show in Figure 8. These four guns are housed in the stainless steel cylindrical vacuum chamber of the sputtering system placed 14cm from the cylinder center (as measured from the target center) and spaced 90° apart. In the present experiment, all samples are either films or repeated bilayers (multilayers), so at most only two guns are required per sample. The guns are covered by a manually controlled rotating chimney assembly. Each gun requires two chimneys. The first is completely covered with Al foil to block the deposition beam from reaching the substrate, thereby protecting an exposed substrate from deposition of unwanted material before its shutter can be closed, for example immediately after a sample has been deposited. The second chimney which has a 5cm diameter hole, is rotated into place while the sample deposition takes place.

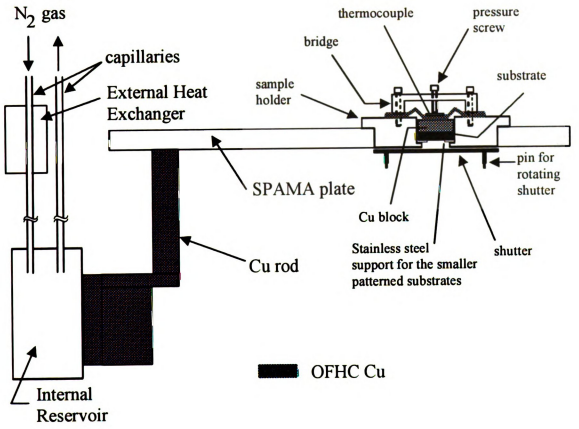

Figure 7 - Schematic cross section of the cooling system with sample holder.

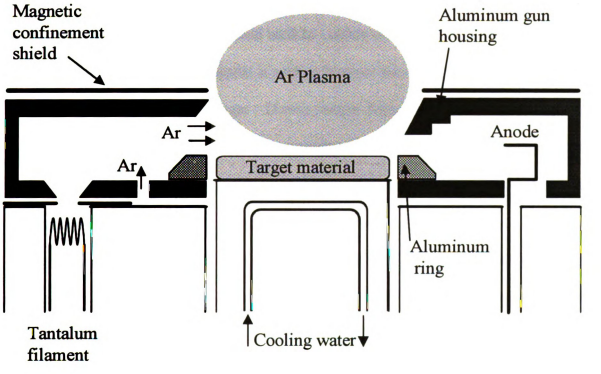

Figure 8 - A cross section of the triode magnetron sputtering gun.

In the sputtering process, ionized Ar atoms are accelerated toward the target. On impact with the target, the kinetic energy of the ion is transferred to target atoms, ejecting them from the target surface. This process results in a diffuse beam of target atoms. The starting gas is 99.999% Ar, passed through a liquid N_2 cold trap, then a gas purifier, and finally forced through several small closely spaced openings at the gun base. The Ar atoms are ionized by establishing an electric current between the anode and the filament. A permanent magnet produces the field used to confine the Ar plasma to the region just above the target. A negative potential is applied between the Ar plasma and the target to accelerate the ions toward the target. During sample deposition, the chimney with the hole limits the ejected material to a beam approximately 5cm across. This constraint on the beam limits unnecessary deposition on system components. Finally a substrate placed 12cm above the target collects some of the target material.

Although material is readily ejected from the target surface, most of the kinetic energy of the Ar ions is deposited in the target as heat. Therefore the target is mounted on a Cu base which is attached to a Cu block containing circulating water to remove the accumulated heat buildup. Once the Ar ions have struck the target, they acquire an electron from the metal surface and are re-emitted as neutral Ar atoms. To provide these electrons in a DC sputtering system, electrically conducting targets must be used.

The sputtering system is computer controlled. The computer directly controls the angular position of the SPAMA plate and performs all the calculations needed to deposit films or multilayers with the proper constituent thicknesses. The computer also monitors the voltage applied to, and the current passing through, the target. The deposition rates

are measured several times during each run using the FTM's, then manually entered into the computer. This information is used by the computer to determine the proper deposition times for the constituent layers.

Before sputtering, the pressure is brought up to 2.5 mtorr by backfilling the chamber with the high purity Ar gas. The pressure is held in dynamic equilibrium throughout the run by flowing Ar at a constant rate through each gun and by opening the gate valve to the pump just enough to maintain 2.5 mtorr. The deposition begins by turning on the necessary sputtering sources and letting them equilibrate, which takes less than 10 minutes. Since no more than two guns are on at any one time, heat buildup on the SPAMA plate is minimized. The target voltages and currents are fixed from run to run for each material so that the deposition rates are similar for samples made in different runs. A schematic of the sputtering system is shown in Figure 9 with typical gun settings and deposition rates listed in Table 1. After the deposition rates are measured and entered into the computer, the shutter below the substrate ready for deposition is manually opened. The sample is rotated to a safe position away from any guns that are on. Then the manually controlled chimney assembly is rotated so the open chimneys are above the targets. When a film is to be grown, the computer rotates the substrate to a position above the desired gun for a time determined by the entered deposition rate and the desired film thickness. Multilayers are grown by rotating the substrate back and forth between two sources. After the sample has been grown, it is again rotated to a safe position and the chimney assembly is rotated so the covered chimneys are above the targets. The shutter is then closed and the sample is protected until it is ready to be removed from the

SI

Fig

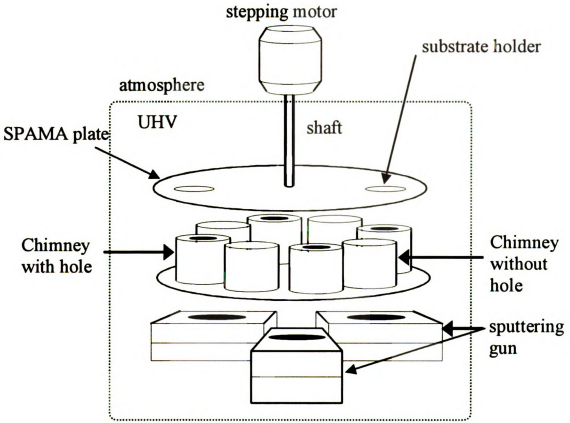

Figure 9 - A schematic of the sputtering system (only three of the four guns are shown for clarity).

sputtering system. Once removed from the sputtering system, samples are stored in a vacuum dessicator to limit surface oxidation.

Sputtering targets are cut to the desired cylindrical shape, 5.72cm in diameter by 0.64cm thick, by the staff of the MSU Physics Shop. Pure Nb and Cu targets are cut from 0.64cm thick plate obtained from Angstrom Sciences.[8] The purity of these bulk materials is 99.95% for Nb and 99.999% for Cu. The CuX alloy targets are cut from alloyed ingots fashioned at MSU using an rf-induction furnace. The alloy targets are made from 99.9999% pure Cu, 99.9% pure Mn, and 99.999% pure Ge, obtained from Aesar/Johnson Matthey Inc.[9] The final Ge and Mn concentrations are determined using EDS on thick sputtered films as described in section 2 of Chapter 3.

Table 1 - Typical gun setting and deposition rates used in this study.

Metal	Target Voltage (V)	Target Current (A)	Deposition Rate (Å/s)
Nb	600	0.7	5.9
Cu	400	0.7	12.2
CuGe(2%)	400	0.7	12.0
CuGe(5%)	400	0.7	11.6
CuGe(10%)	400	0.7	10.7
CuMn(0.3%)	400	0.7	10.9

An acid etch consisting of a mixture of 50% HNO_3 and 50% deionized water is used to clean most of the parts of the sputtering system. These include the sample holders, sample shutters, SPAMA plate, sample supports (for the patterned substrates), gun bodies, and the Al target confinement rings. Deposits not readily removed by the acid are scrubbed vigorously with an iron wire brush and then re-etched. Nb proved to be very difficult to remove from the gun parts because the Al gun parts etched away nearly as fast as the unwanted Nb deposits. Therefore a razor blade is used to scrape away most of the Nb, after which approximately 5% HF is added to the acid solution to help remove the rest. Since stainless steel is unaffected by HF, all stainless steel parts are etched in the HNO_3, deionized water, and HF solution. After the acid etch, all these parts are rinsed in deionized water and sequentially washed ultrasonically for 5 minutes in acetone, and dehydrated ethyl alcohol. The SPAMA plate is too large to fit in the ultrasound bath so it is rinsed by hand with acetone and alcohol. Each gun part is only used with a designated type of target to minimize the possibility of cross contamination. The chimneys are never cleaned directly, but before each run they are covered with Al foil which is discarded at the end of the run. The magnetic confinement plates, sample bridge assemblies, Cu heat sink blocks, and thermocouples are also not cleaned before each run, but kept clean between runs. These components are not cleaned because they are either, never in contact with the sputtered metal beam (and therefore have no significant deposits on them), are not in close proximity with the polished face of the substrate, or are highly reactive in all acids and so are discarded when their deposits become severe, which is the case for the magnetic confinement plates, which are made of iron.

Chapter 3

SAMPLE CHARACTERIZATION

All of the samples used in these experiments were either films or multilayers. The multilayers were of the form Nb/CuX, where CuX was either pure Cu, CuGe(2%), CuGe(5%), CuGe(10%), or CuMn(0.3%). The purpose of sample characterization was to determine or verify the structure of the samples. What is the actual Ge or Mn concentration in the Nb/CuGe and Nb/CuMn multilayers? Were the layer and film thicknesses as expected from the sputtering conditions? These were just a few of the questions addressed in the analyses. To answer these and other questions posed about the structure of the samples three basic apparatuses were used. The CFMR (Center for Fundamental Materials Research) Rigaku powder x-ray diffractometer was used to check the layer thicknesses. EDS (Energy Dispersive Spectroscopy) measurements were taken on a JOEL JSM-6400 SEM to check the concentration of impurities in the CuX layers. Measurements of the surface profile of the patterned samples were made with a Sloan Dektak IIA.

In this chapter, the results of these measurements are discussed.

3.1 XRD

Most of the x-ray diffraction data were taken and analyzed by M. L. Wilson. Details of the diffractometer and several data sets are found in his dissertation[10]. He found the bilayer separation Λ of the multilayers to be within 5% of their expected value, and the rms deviations of the Nb and CuX layer thicknesses to be no larger than 3Å. The Nb and CuX layers are crystalline and preferentially oriented with the Nb bcc (110) and the CuX fcc (111) planes parallel to the substrate surface to within 5°.

All of the x-ray studies were made on non-patterned samples. Also the bilayer separation had to be $\leq$ 100Å to identify the Bragg peaks from the layering of the sample. Since the Nb layer was fixed at 280Å, such measurements could not be performed on the multilayers used in this study but similar results were assumed for these thicker layered samples.

3.2 EDS

EDS is used to determine the concentration of desired and undesired impurities in the layers. The EDS measurements are performed on a JOEL JSM-6400 SEM. EDS measures the elemental composition of a sample by exciting the atoms in the sample with a high energy electron beam. For this study a 15 kV accelerating voltage is used. The relative fluorescent x-ray line intensities are then compared using a standardless analysis program to obtain the relative atomic percentages. Table 2 lists the EDS results of all

Table 2 - EDS results of all CuX film types.

CuX Type	Cu Wt%	Impurity Wt%	
Cu	100%	None	
CuGe(2%)	98.00±0.05	Ge	2.00±0.05
CuGe(5%)	95.10±0.10	Ge	4.90±0.10
CuGe(10%)	89.85±0.11	Ge	10.15±0.11
CuMn(0.3%)	99.73±0.05	Mn	0.27±0.05

CuX type films used in this study. The EDS data showed no evidence for unwanted impurities in either the Nb or CuX films above the detection limit of the method (less than 0.1 at.%). However a beryllium window located inside the collimator absorbs lower energy x-rays and prohibits the detection of elements with atomic number ≤ 11.

3.3 Surface Profiles of Patterned Samples

A Sloan Dektak IIA was used to obtain surface profiles of the patterned samples to determine the width of the wire. In Figure 10 is a SEM image of a wire in a 5000Å Nb film. The same wire is profiled in Figure 11. The profile shows that the wire width at half height is 50μm. The SEM image shows an edge roughness of about ±3μm. All patterned samples similarly checked are consistent with a wire width of 50±3μm.

The surface profiles also provide a check on the film thicknesses expected from the sputtering conditions. As seen in Figure 11, the film is measured to be 5000Å thick,

exactly as expected from the sputtering conditions. All similarly checked films were well within 5% of their expected value, in agreement with the XRD results.

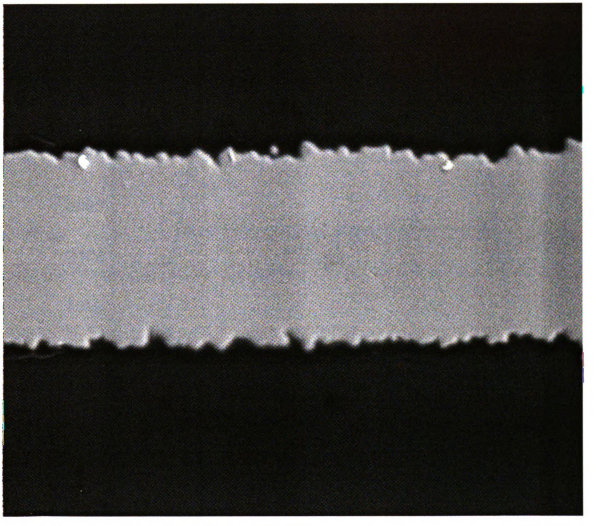

Figure 10 - A SEM image of a wire in a 5000Å Nb film. The wire is 50μm wide.

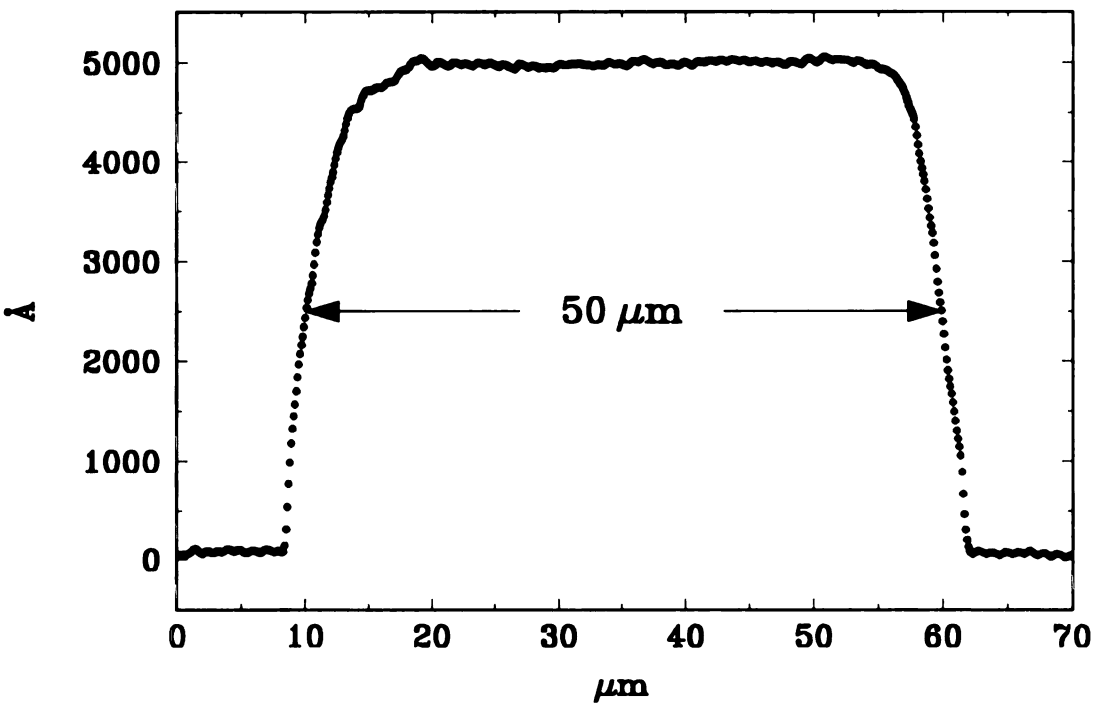

Figure 11 - A profile of a wire in a 5000Å Nb film obtained on a Sloan Dektak IIA.

Chapter 4

EXPERIMENTAL PROCEDURES

The experimental results reported in this thesis were obtained from magnetization and critical current measurements. Both measurements were made using a Quantum Design[11] Magnetic Property Measurement System (MPMS). The magnetization measurements used the system's SQUID magnetometer circuits and the MPMS control software. The critical current measurements used the MPMS as a computer controlled gas flow cryostat and magnetic field platform. The control software was also used to run External Device Control (EDC) programs that controlled a Keithley[12] 224 Programmable Current Source and a Keithley 182 Sensitive Digital Voltmeter.

The mounting of the samples for magnetization and critical current measurements, and the data taking procedures will be described in the remainder of this chapter. Illustrative data will also be shown.

4.1 Magnetization Measurements

Magnetization measurements are made using the MPMS's superconducting quantum interference device (SQUID) system. The SQUID is coupled to a series of pickup coils, wound in a second derivative configuration in which the upper and lower single turns are counterwound with respect to the two-turn center coil. This configuration strongly rejects interference from nearby magnetic sources. The separation between the top and bottom coils is 3cm. A measurement is taken by moving the sample through the pickup coils, in a 4cm scan centered on the two-turn center coil. Throughout the scan the SQUID voltage is read and a SQUID response versus sample position curve is generated. This scan is generally repeated 3 times and the 3 curves averaged. The average curve is fit with a theoretical form and the best fit is used to calculate the sample magnetization in EMU. The standard deviation is determined from the variation in the 3 scans. Figure 12 illustrates the core of the MPMS. Figure 13 is a screen capture from the MPMS control software illustrating the SQUID response versus sample position curve.

The above calculations are all internal to the MPMS control software. The control software is also used to generate a list of system commands such as setting the temperature or field. A generated list of these commands is called a sequence. Once a sample is mounted, loaded into the system, and a sequence started, the system can be left unattended until the sequence finishes. The user will return and find his data (T, H, χ, $\Delta\chi$, etc.) tabulated in a file on the system's computer.

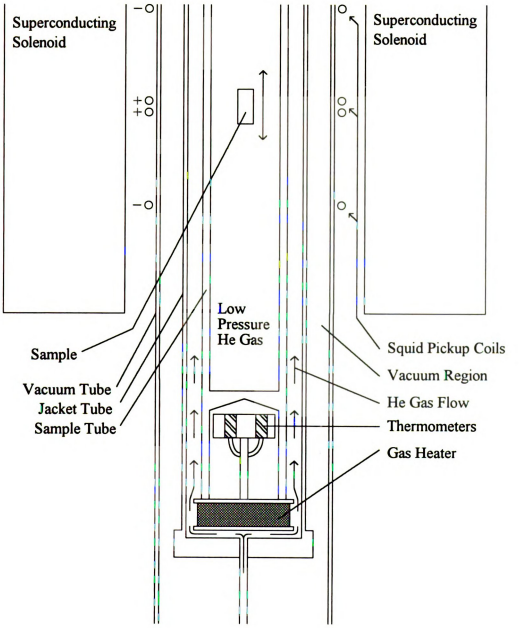

Figure 12 - The core of the MPMS.

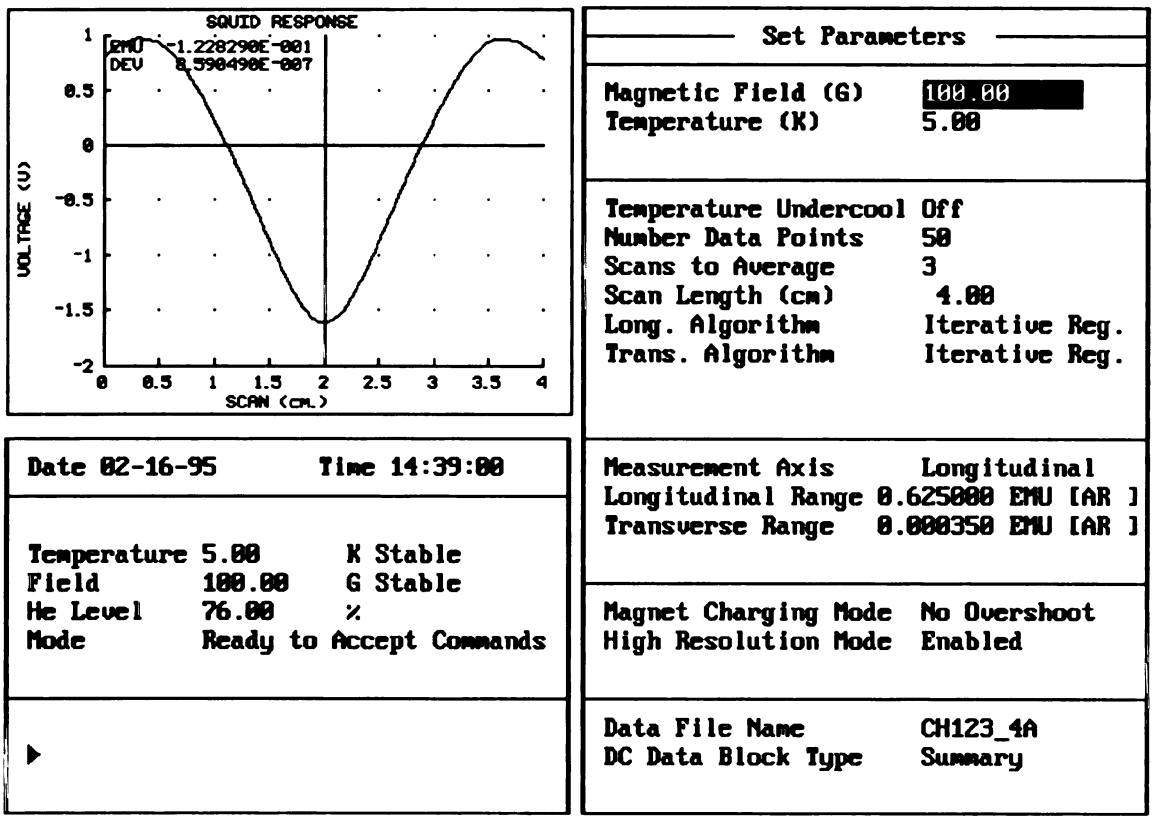

Figure 13 - A screen capture from the MPMS control software. The negative squid response as the sample moves through the center pickup coil, the 2cm mark, indicates diamagnetic behavior.

For temperature control, the sample is placed in 1 mtorr He exchange gas, which determines the sample temperature by coupling the sample to the He gas from the main reservoir of the system. This gas is pumped past a heater and around the sample chamber. The temperature is monitored by a pair of thermocouples in a different exchange gas also separated from the pumped gas. The field is controlled by regulating the amount of current supplied to a superconducting solenoid that encompasses the cylindrical sample chamber. This solenoid generates a field directed along the central axis of the sample chamber.

This measurement technique can cause problems in extracting the magnetization of a superconducting sample[13,14], because the sample is moved during the measurements. A small inhomogeneity in the applied field or temperature over the sample path can produce very misleading results. These concerns determined the 4cm scan length, since the "apparent" magnetization proved to be independent of scan length for scans of 4cm or less.

The sample is mounted inside a suprasil quartz tube[15] suspended from the bottom of a sample rod supplied by Quantum Design. The tube has an inner diameter of 6.75mm, an outer diameter of 7.5mm, and is 20cm long. Kapton tape[16] is wrapped around the base of the sample rod to match the inner diameter of the tube. The tube is slid over this tape for support. About 6.5cm from the bottom of the tube are 8 small holes, through which white thread is passed to support the sample. The holes, which were cut by the MSU glass shop, are divided into 2 planes with 4 holes each. The 2 planes are separated by 0.35mm or about the thickness of the sample substrates. For insertion into the tube, a

4.5mm square sample is cleaved from the half inch square sample created in the sputtering system. Once in the tube, the sample is tied into place with white thread. The sample is now ready to be loaded into the MPMS. For this experiment two sample orientations are used, one with the applied field perpendicular to the plane of the sample and the other with the applied field in the sample plane. Figure 14 shows a sketch of a sample mounted in both orientations.

Before the sample is lowered down the sample column, it is put into a loading airlock which is purged several times with He gas. The superconducting solenoid is also soft quenched to remove any remnant fields left by the last user of the system. The sample is lowered down the sample column and the temperature is allowed to stabilize at 5K. The 4cm scan length is then centered on the center SQUID pick up coil.

With the sample in place, a sequence to determine the irreversibility temperature as a function of applied field, $T_{irr}(H)$, can be started. The sequence repeats a series of zero field cooled (ZFC) and field cooled (FC) temperature sweeps for a number of different fields. The sequence is programmed to start by warming the sample to above T_c and cooling the sample to well below T_c in zero field. The field is then applied and magnetization measurements are made in increments of 0.05K as the temperature is raised. These measurements make up the ZFC temperature sweep. Once the temperature is several tenths of a degree above T_c, magnetization measurements are again made every 0.05K as the temperature is lowered. These measurements make up the FC temperature sweep. The FC measurements continue until a clear divergence is seen between the two temperature sweeps. The field is then turned off, the temperature set to above T_c, and the

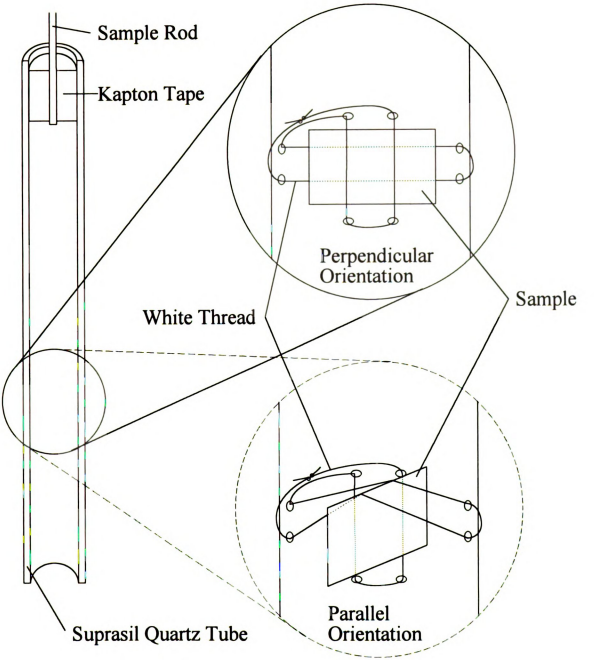

Figure 14 - Samples mounted for magnetization measurements.

sample again zero field cooled. The field is then raised to the next desired field value and the process is repeated. The desired field values are always set in increasing order to minimize the effect of remnant fields.

Typical ZFC and FC data are displayed in Figure 15. T_c is defined as the onset of diamagnetism and T_{irr} is the temperature below which the magnetization is irreversible.

4.2 Critical Current Measurements

All critical current measurements are also taken in the DC MPMS which allowed measuring fields up to 5.500×10^4G. Since the same apparatus is used for these measurements, the temperature and field is controlled exactly as described in the previous section. There is the added benefit that the sample is stationary during the measurement, meaning the sample is not exposed to the small inhomogeneity in the applied field or temperature over a sample path. For a critical current measurement, the MPMS control software is used to run external device control (EDC) programs. The two external devices controlled by these programs are a Keithley 224 Programmable Current Source and a Keithley 182 Sensitive Digital Voltmeter. The EDC programs set the current from the current source and read the voltage from the digital voltmeter. The user will return and find his data (T, H, I, and V) tabulated in a file on the system's computer.

The sample is mounted at the bottom of a special EDC sample rod supplied by Quantum Design, which contains small Cu wires for the electrical measurements. Two such sample rods are used in this study, one for parallel measurements and another for

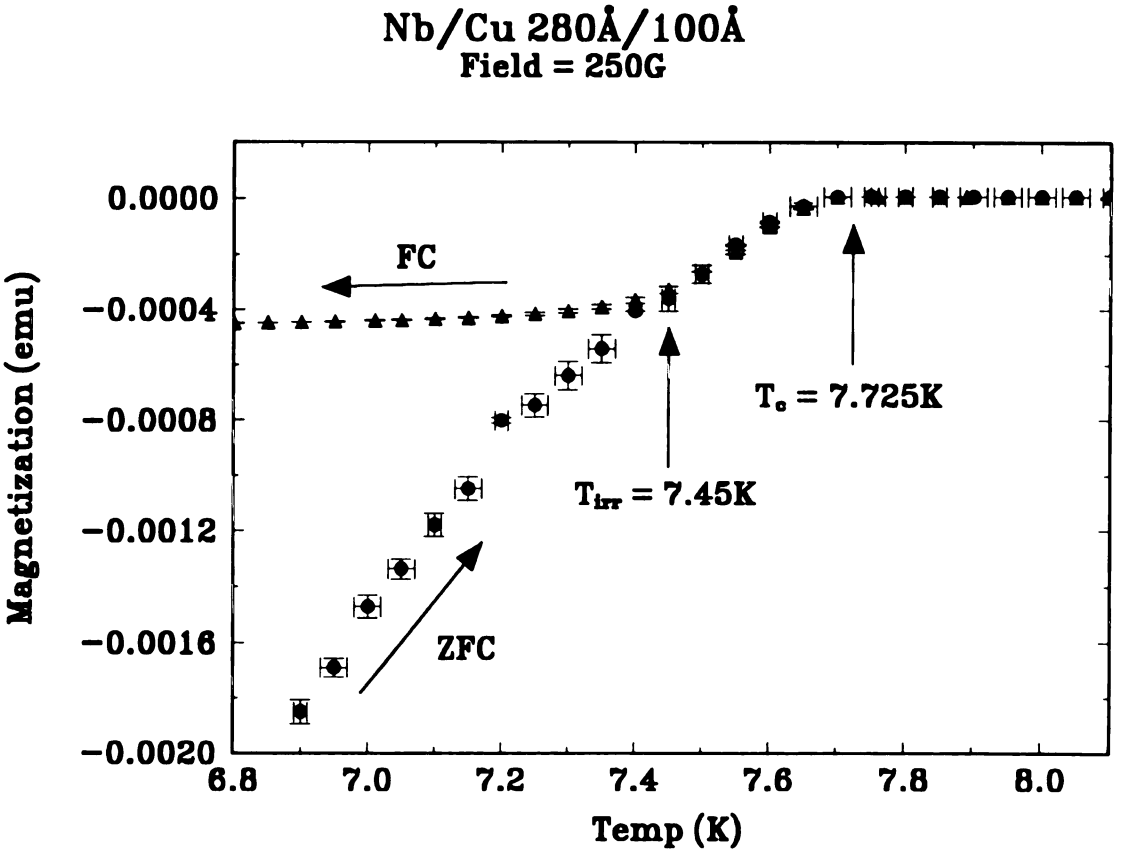

Figure 15 - A typical set of ZFC and FC magnetization curves.

perpendicular measurements. Figure 16 shows a sketch of a sample mounted in both orientations. The sample is heat sunk to a large metal platform at the bottom of the sample rod with a small amount of Apiezon M Grease[17]. Electrical contact is made to the sample using silver paint to connect the two current leads to the current contact pads, and the two voltage leads to the voltage contact pads. Once the silver paint has dried, the sample is ready to be loaded into the MPMS.

As before, the sample is put in the loading airlock, which is purged several times, and the superconducting solenoid is soft quenched to remove any remnant field. The sample is lowered down the sample column slowly to avoid rapid sample cooling which may cause the silver paint electrical contacts to come loose. The sample is then stabilized at 5K and positioned close to the center SQUID pick up coil. The SQUID is not used in these measurements, but the center pick up coil also marks the center of the superconducting solenoid.

With the sample in place, an EDC program is started. This program records the measured voltage for an applied 0.1 mA current in zero field as the temperature is increased in increments of 0.02K. The program starts at a temperature below T_c and continues increasing temperature until a sharp rise appears in the recorded voltage well above the noise level (typically ~ 0.5μV) of the measurement. The onset of this sharp rise characterizes T_c of the sample. The measured T_c is then put into the second EDC program, which measures the critical current as a function of applied field and temperature. This procedure helps maximize the efficiency of the program, which can take up to 3 days to collect a complete set of critical currents. This second program starts

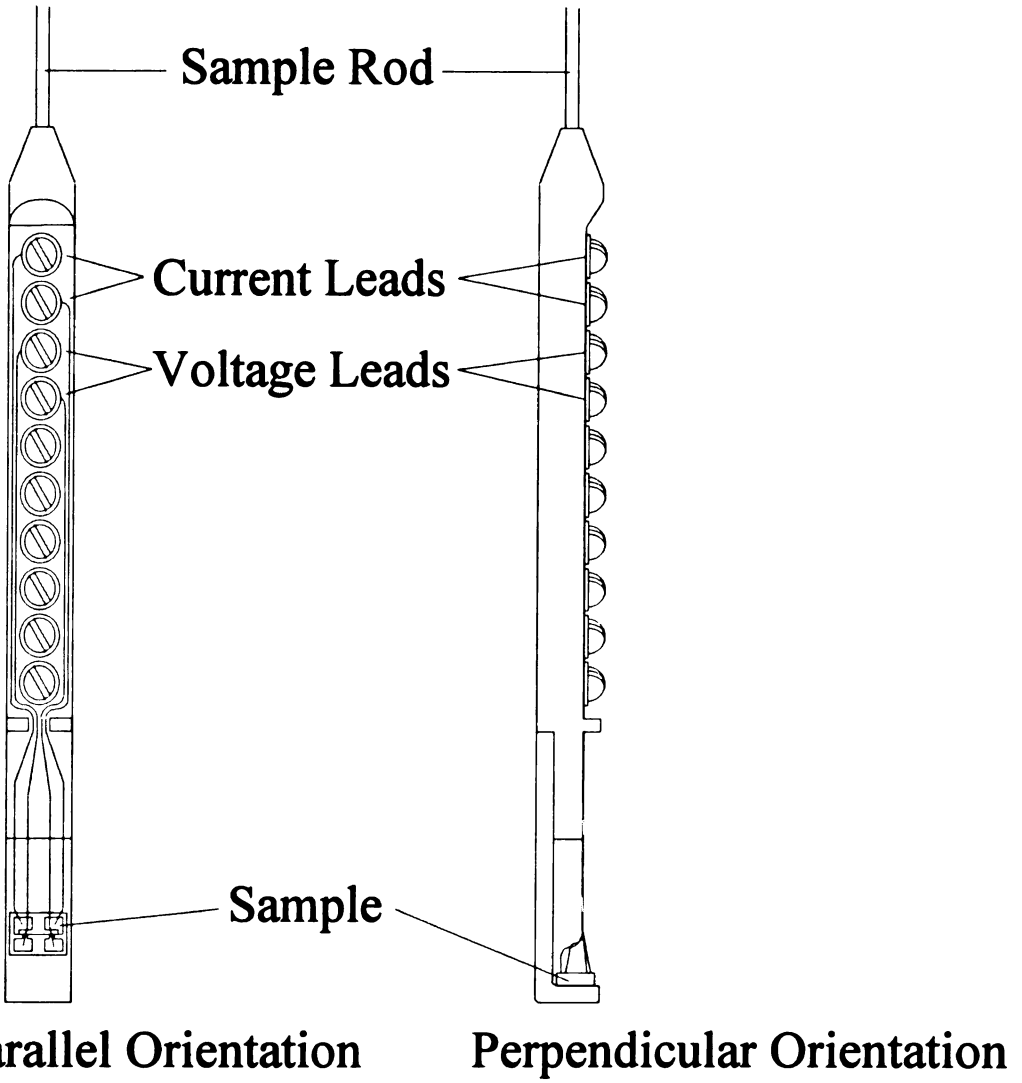

Figure 16 - Samples mounted for critical current measurements.

in zero field and measures the critical current in 0.2K steps from 5K up to T_c. Once the first temperature sweep is done, the field is set to the first desired field setting and the temperature sweep repeated. This time measurements are only made up to $T_c(H)$. The next field is then set and the process repeated until $T_c(H)$ is less then 5K. At any given temperature and field setting, the critical current is determined by increasing the applied current until a specified voltage is reached, in this case 10 μV. The current is increased in 0.1 mA increments from 0.1 mA to 10 mA and in 1 mA increments after that if necessary. The critical current is defined as the largest current which produced a measured voltage of less then 0.5 μV. Figure 17 shows a typical current sweep with the critical current indicated.

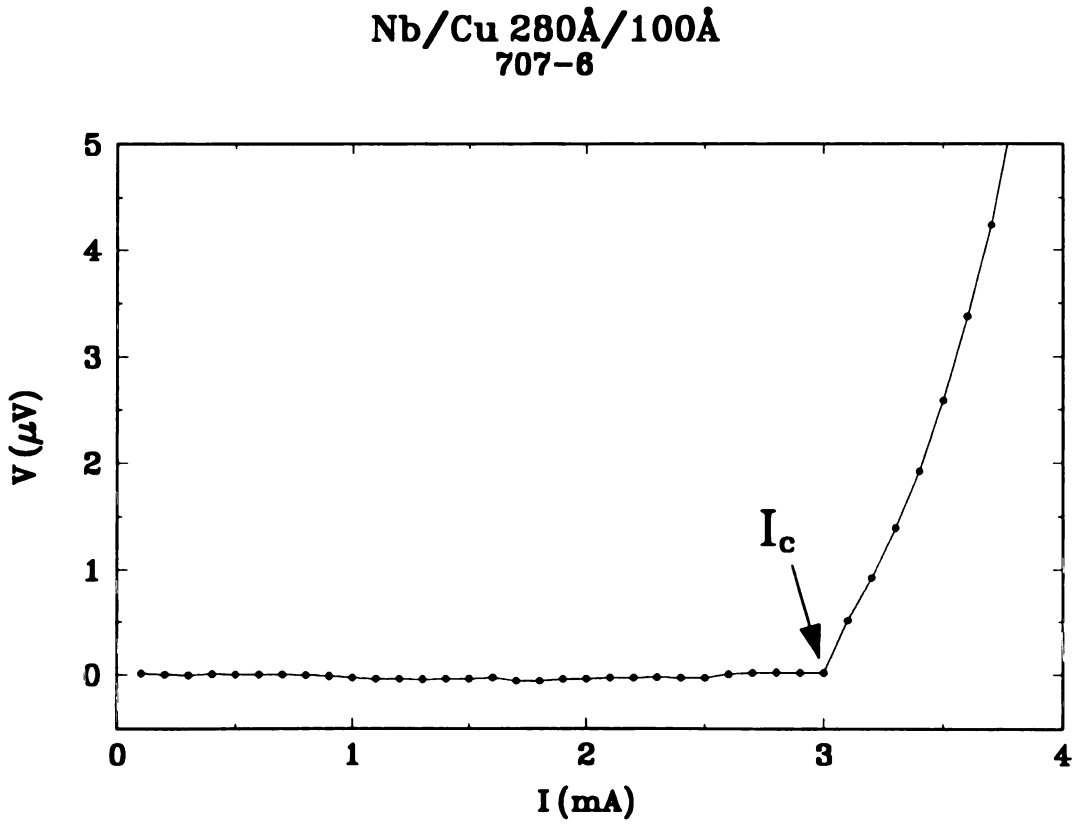

Figure 17 - A typical current sweep, this one taken at 5.6K and 600G.

Chapter 5

THE MAGNETIZATION IRREVERSIBILITY LINE

Irreversibility has been seen in many superconductors, from the high-T_c ceramics[18,19,20] to Niobium films[14]. It can be defined simply as the separation of the zero field cooled (ZFC) and the field cooled (FC) magnetization curves. For the ZFC magnetization curve, the sample is cooled to below T_c in zero magnetic field and a measuring field is applied to measure the magnetization as a function of increasing temperature. For the FC magnetization curve, the sample is cooled in the measuring field as the magnetization is measured. Figure 15 is an example. In the ZFC case, there are no vortices in the sample before the measuring field is applied. As the field is applied, flux enters the sample in the form of vortices which become pinned due to the presence of defects or other pinning centers present in the sample. These pinning sites prevent more vortices from entering the sample, and are responsible for the large diamagnetic signal of the sample. In the FC case since the flux was already in the sample as it was cooled, the sample is less diamagnetic. The same pinning sites now prevent vortices from being expelled. This irreversibility will go away at a temperature $T_{irr} < T_c$ where the thermal energy is sufficient to unpin the vortices.

In this chapter, the theory behind the field dependence of T_{irr}, known as the irreversibility line, $T_{irr}(H)$, will be outlined. Experimental data will be used to address the

ongoing debate over whether this history-dependent property is associated with flux creep, a glass transition, or vortex-lattice melting. The results of irreversibility measurements performed on Nb/CuX multilayers in two sample orientations will be shown.

5.1 Theory

The three most significant theoretical models regarding the irreversibility line, $T_{irr}(H)$ or $H_{irr}(T)$, involve flux creep, a transition from a vortex glass to a vortex liquid, or a transition from a vortex lattice to a vortex liquid. The flux creep model, presented by Yeshurn and Malozemoff[18], says that the irreversibility line is the result of the thermally activated depinning of the vortices and predicts:

$$1 - t = \left(\frac{8\pi f^2 B k T_c \ln(Bd\Omega/E_c)}{2.56 H_{c2_0}^2 \Phi_0 \xi} \right)^{2/3} . \qquad \text{Equation [1]}$$

Here $t = T/T_c$ is the reduced temperature, B the magnetic induction, d the average distance between pinning centers, Ω the oscillation frequency of a flux line in a pinning well, E_c the electric field determined from the lowest measurable voltage divided by the sample length, f the ratio of the penetration depth to the flux lattice spacing, Φ_0 the flux quantum, and ξ the superconducting correlation length. For parameters typical of conventional low-temperature superconductors, $\ln(Bd\Omega/E_c)$ is about 30. Near T_c, where the field B is approximately H, this equation is of the form:

$$H_{irr}(T) = H_{irr_0}\left(1 - \frac{T}{T_c}\right)^{3/2} \qquad \text{Equation [2]}$$

where H_{irr_0} is a constant.

The same 3/2 power law behavior is expected for the melting of a vortex glass. This behavior is expected by analogy with the Almeida-Thouless[21] line in spin-glasses, describing the melting of a similar glass-like state. Both systems are frustrated. The spin-glass system is frustrated by a random coupling constant. The frustration in the vortex glass is due to the competition between the desire to form a triangular array of vortices which minimizes the vortex-vortex interaction energy, and the randomness of the pinning sites.

Houghton, Pelcovits, and Subdø[22] have derived an expression for the vortex lattice melting line of a uniaxially anisotropic material:

$$\frac{t}{\sqrt{1-t}}\frac{\sqrt{b}}{1-b}\left(\frac{4\left(\sqrt{2}-1\right)}{\sqrt{1-b}}+1\right) = \alpha \qquad \text{Equation [3]}$$

where α, the degree of susceptibility of the vortices to thermal motion, is given by:

$$\alpha = 2\times 10^5\left(\frac{c}{\kappa}\right)^2\left(\frac{H_{c2_0}}{T_c^2}\frac{M}{M_z}\right)^{1/2}. \qquad \text{Equation [4]}$$

Here $t = T/T_c$, $b = H/H_{c2}(T)$, $H_{c2}(T) = H_{c2_0}[1 - T/T_c]$, $\kappa \cong \lambda/\xi$ is the Ginzburg-Landau parameter, the lengths λ and ξ are the penetration depth and correlation length respectively, and M/M_z is the ratio of the in-plane and out-of-plane effective masses. The Lindemann criterion for melting is governed by the parameter c, which is the ratio of the

mean-square thermal displacement of the vortices from their equilibrium positions to the vortex lattice spacing. For T near T_c it can be shown that the melting curve is given by:

$$H_{irr}(T) = H_{irr_0}\left(1 - \frac{T}{T_c}\right)^2 \qquad \text{Equation [5]}$$

which has the same functional form as the prediction made by the two previous models, with a different exponent.

The transition at T_{irr} is believed to be highly sensitive to disorder, being either first order or continuous depending on the number, type, and geometry of impurities. Although there is a good grasp[10] on how these various impurities affect T_c, there is a lack of theoretical predictions for their effects on T_{irr}. For thick Cu interlayers, T_c is reduced from what it would be for an isolated Nb film because Cooper pairs leak into the interlayers by the proximity effect. As the Cu layers get thinner the T_c of the multilayer, T_{cSN}, goes up because some of the Cooper pairs pass all the way through the Cu layer and enhance the pair density in adjacent Nb layers. T_c can also be raised by adding Ge impurities to the Cu. These don't destroy the Cooper pairs, but they tend to reflect the pairs back into the Nb layer from which they came, again enhancing the pair density in Nb. The addition of Mn destroys most of the Cooper pairs that enter the interlayer and dramatically reduces T_{cSN}. In Figure 18 is shown a schematic version of the three dominant processes for a Cooper pair entering a normal metal interlayer.

A theoretical interest addressed in this study is the proposed[23] 3D to 2D transition that occurs in high-T_c materials at high field with the applied field oriented perpendicular

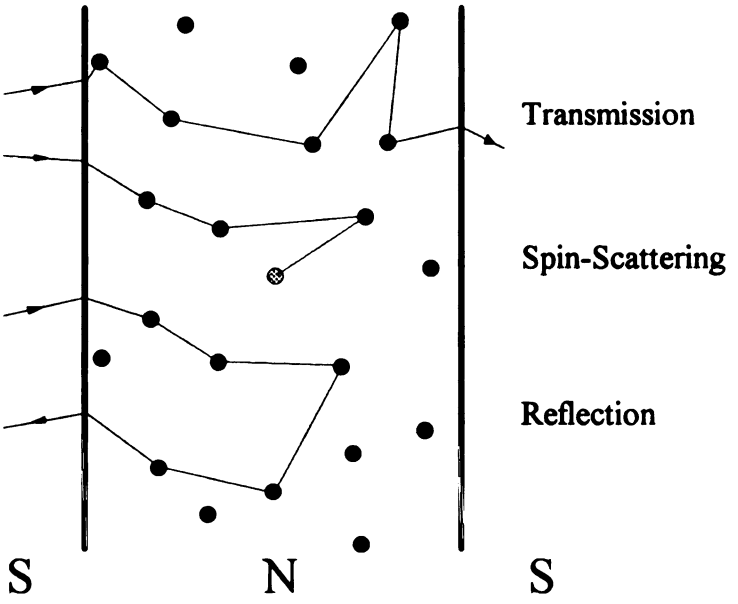

Figure 18 - The three dominant processes for a Cooper pair entering a normal metal layer.

to the CuO planes. At high fields, as the density of vortices gets high, it is thought that the vortex-vortex interaction within the layers overcomes the interaction between the layers, causing the 3D line vortices to breakup into 2D pancake vortices. The high field destroys or severely weakens the proximity induced superconductivity in the N layers. If this happens, increased pinning, which would normally increase T_{irr}, might not have much of an effect, since a pinned pancake has no effect on pancakes in other layers, whereas a pinned line vortex affects many layers. If this effect can be seen in the Nb/CuX multilayers, it should be possible to control the field at which this transition takes place. By adding impurities, either Ge or Mn, the interaction between vortices in adjacent layers can be weakened causing the 3D line vortices to breakup into pancake vortices at lower

fields. There are however currently no theoretical predictions on how this transition will affect the shape of $T_{irr}(H)$ in the phase diagram.

Another theoretical question which arises is what to expect for the behavior of T_{irr} when the multilayer sample is parallel to the field. It is known[10] that in the parallel orientation a 3D/2D/3D crossover can be seen in $H_{c2}^{\parallel}(T)$ as the temperature is lowered. H_{c2} in bulk materials is reached when the area available per flux quantum approaches $2\pi\xi^2$, twice the area of the normal region surrounding a vortex. Therefore $H_{c2} = (\Phi_0/2\pi\xi^2)$ where Φ_0 is a flux quantum and ξ is the coherence length perpendicular to the field. Since multilayers are not isotropic, when the field is applied parallel to the layers one must consider two ξ's, a ξ_{xy} parallel to the layers, and a ξ_z perpendicular to the layers. In these multilayers where $H_{c2} \propto 1/\xi_{xy}\xi_z$, the temperature dependence follows one of three trends. Near T_c both ξ's diverge as $\xi \propto (1 - T/T_{cSN})^{-1/2}$ so 3D behavior is observed with $H_{c2} \propto (1 - T/T_{cSN})^{1}$. As T decreases, ξ_z is limited by d_S and 2D behavior is seen with $H_{c2} \propto (1 - T/T_{2D})^{1/2}$ and finally at a still lower temperature where both ξ's are small compared to d_S, H_{c2} behaves as in the bulk S material:

$$
\begin{aligned}
&T_{2\leftarrow 3} < T < T_{cSN} && H_{c2}^{\parallel} \propto \left(1 - T/T_{cSN}\right) && \\
&T_{3\leftarrow 2} < T < T_{2\leftarrow 3} && H_{c2}^{\parallel} \propto \left(1 - T/T_{2D}\right)^{\upsilon} && \upsilon \cong 1/2. \qquad \text{Equation [6]} \\
&T < T_{3\leftarrow 2} && H_{c2}^{\parallel} \cong H_{c2}^{\text{bulk}}(T) &&
\end{aligned}
$$

Here $T_{2\leftarrow 3}$ is the 3D to 2D dimensional-crossover temperature, T_{2D} is the effective T_c for the 2D regime, $T_{2\leftarrow 3}$ is the crossover temperature from 2D to bulk behavior, and $H_{c2}^{\text{bulk}}(T)$ is H_{c2} for bulk S.

The $H_{c2}^{\perp}(T)$ curve of a Nb 280Å / CuGe(5%) 200Å multilayer as determined from resistance measurements is shown in Figure 19[10]. No theoretical work has been done to determine how this dimensional crossover will affect the behavior of T_{irr}.

Another controversy involves how best to experimentally determine the irreversibility line[24]. One method is to use the field cooled (FC) and zero field cooled (ZFC) dc magnetizations. Upon increasing the temperature, the joining of the ZFC and FC curves (recorded at a field H_0) takes place at a temperature T_0 giving a point on the irreversibility line, $H_{irr}(T_0) = H_0$. The obvious experimental limit of this technique is the noise in the data[25], since T_0 is the temperature at which the difference in the ZFC and FC magnetizations becomes greater then the noise. As the two magnetizations are smoothly joining curves, the error bars in T_0 are important and difficult to determine experimentally.

Another experimental technique[26] used to determine the irreversibility line is the maximum in the out-of-phase component $\chi''(T)$ of the ac susceptibility at a temperature T_{max}, recorded at a low frequency and at some small ac field amplitude superimposed on a large dc field H_0. Here T_{max} determines $H_{irr}(T)$ by the relation $H_{irr}(T_{max}) = H_0$. Others[27] have used the onset temperature of $\chi''(T)$ instead of T_{max} in the above relation. The absorption χ'' is proportional to the ac magnetization hysteresis loop area, which is non-zero in the presence of irreversibility. Therefore irreversibility should exist above T_{max}. Based on the above arguments, the use of the $\chi''(T)$ onset criteria should be more consistent than the use of the $\chi''(T)$ maximum criteria. However, skin depth penetration effects also give non-zero $\chi''(T)$ values. All these complications produce frequency and ac amplitude dependencies in $\chi''(T)$ which shouldn't be present if the irreversibility line

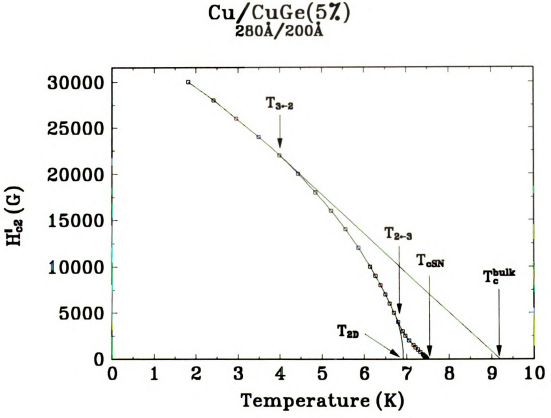

Figure 19 - The 3D/2D/3D transition seen in $H^{\perp}_{c2}(T)$.

probes a critical phenomena like the melting of a vortex solid. Therefore the physical meaning of the ac irreversibility line remains unresolved. While the dc technique lacks accuracy, there is less dispute over the validity of the dc irreversibility line. There exist other determinations of $H_{irr}(T)$ using electric transport properties, but the presence of Lorentz forces adds further complications to those of the magnetic studies.

5.2 Experimental Results

For this study the "dc" technique was used. The ac technique was tried but produced irreproducible results and was abandoned. Transport measurements were also made to look for $H_{irr}(T)$ but with the available system only $H_{c2}(T)$ could be seen. Below $H_{c2}(T)$ the measured resistance of the sample dropped below the inherent noise of the system (about 10^{-6} ohms) and no irreversibility could be seen. One concern that can be raised about measuring the dc magnetization in a Quantum Design SPMS is the motion of the sample during the measurement. Since the MPMS requires the sample to move through a non-uniform field, it can be thought of as imposing a small amplitude ac field on the measurement with a period of the measurement time (about 2 minutes).

Figure 15 is a graph of the ZFC and FC magnetization curves of a Nb 280Å / Cu 100Å sample in an applied perpendicular field of 250G. Figure 20 is an illustration of the difference between successive data points on the FC magnetization curve, which shows the characteristic sharp rise at T_c. Figure 21 illustrates the difference

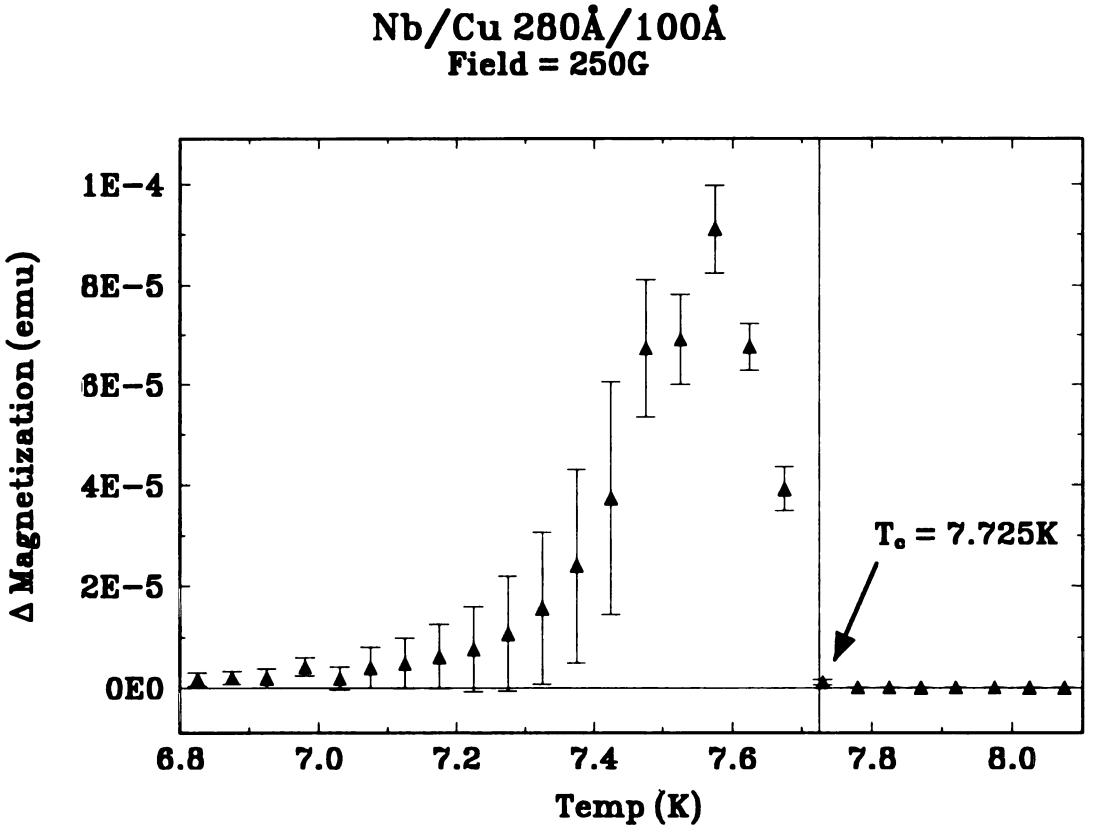

Figure 20 - The differences between successive data points on a FC magnetization curve graphed to illustrate the sharp rise at T_c.

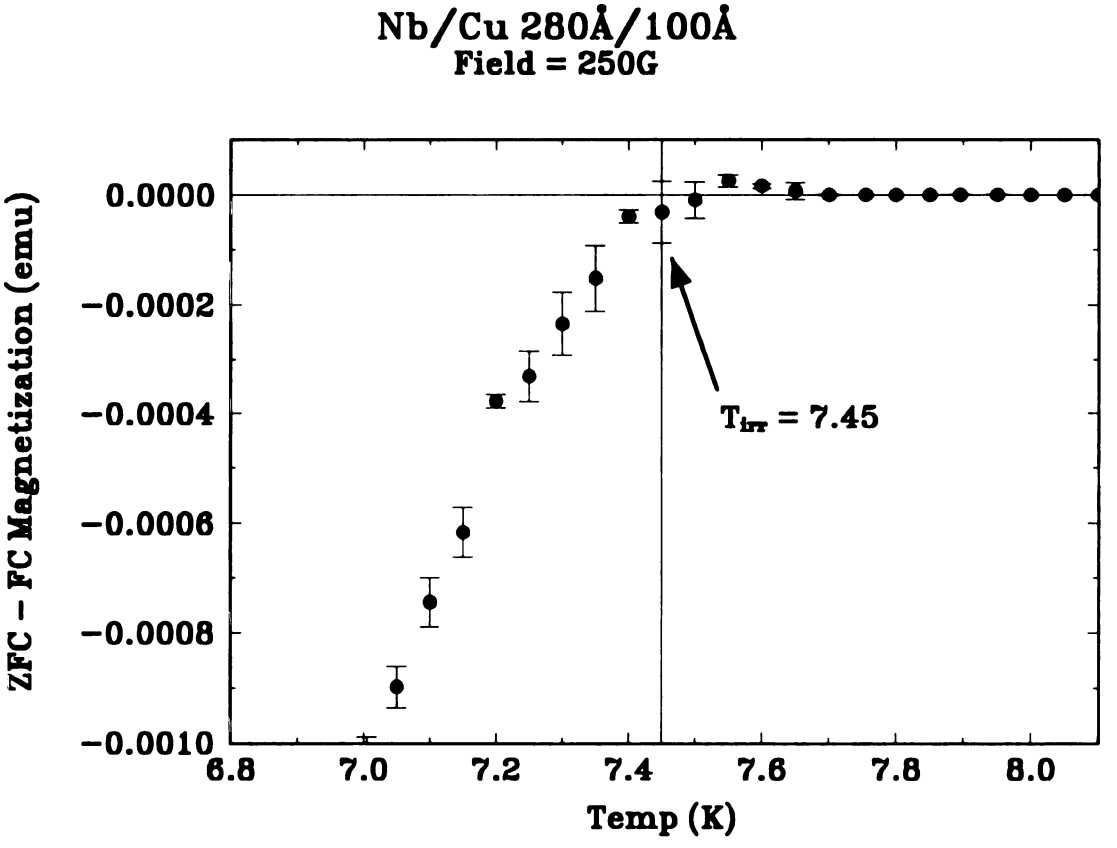

Figure 21 - The difference between FC and ZFC data points measured at the same temperature graphed to illustrate the sharp drop at T_{irr}.

between FC and ZFC data points measured at the same temperature versus measuring temperature. Here the characteristic sharp drop is seen at T_{irr}.

The $T_c(H)$ and $T_{irr}(H)$ data for all samples were then fit with:

$$H_{c2}(T) = H_{c2_0}\left(1 - \frac{T_c}{T_{c_0}}\right)^{P_c} \text{ and } H_{irr}(T) = H_{irr_0}\left(1 - \frac{T_{irr}}{T_{c_0}}\right)^{P_{irr}} \qquad \text{Equation [7]}$$

with H_{c2_0}, P_c, H_{irr_0}, P_{irr} and T_{c_0} as fitting parameters. Both data sets were fit simultaneously since T_{c_0} was a parameter in both equations.

$H_{c2}(T)$ was also determined from transport measurements for a few samples. Good agreement was found between the transport and magnetically determined parameters. See Figure 22 for a graph of both $H_{c2}^{\perp}(T)$ curves and the $H_{irr}^{\perp}(T)$ curve of the Nb 280Å / Cu 100Å sample.

5.2.1 Perpendicular

All samples measured in the perpendicular orientation are listed in Table 3. Table 4 contains the previously mentioned fitting parameters obtained from the data for these samples. Figure 23 through Figure 25 show the H-T phase diagrams for several of these samples. Figure 26(a) is a graph of H_{c2_0} and H_{irr_0} versus the normal metal layer thickness, d_N, for the Nb/Cu multilayers. The $d_N = 0$ point was obtained from a measurement on the 5000Å film. Figure 26(b) is a similar graph for the P_c and P_{irr} parameters. Figures 27 through 29 are similar to Figure 26 except they display the

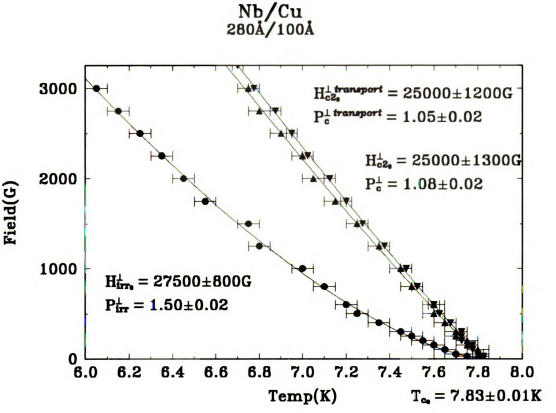

Figure 22 - $H_{c2}^{\perp}(T)$ determined from magnetization measurements (▲) and transport measurements (▼) along with $H_{irr}^{\perp}(T)$ determined magnetically (●).

Table 3 - All samples measured with H perpendicular to the multilayers.

Sample Number	Sample Description
456-16	5000Å Nb Film
360-7	Nb 280Å / Cu 20Å
360-9	Nb 280Å / Cu 40Å
360-11	Nb 280Å / Cu 100Å
360-13	Nb 280Å / Cu 200Å
440-7	Nb 280Å / Cu 400Å
360-12	Nb 280Å / Cu 700Å
622-3	Nb 280Å / CuGe(2%) 20Å
622-4	Nb 280Å / CuGe(2%) 40Å
622-5	Nb 280Å / CuGe(2%) 60Å
622-6	Nb 280Å / CuGe(2%) 80Å
622-7	Nb 280Å / CuGe(2%) 100Å
622-8	Nb 280Å / CuGe(2%) 150Å
622-9	Nb 280Å / CuGe(2%) 200Å
622-10	Nb 280Å / CuGe(2%) 300Å
622-11	Nb 280Å / CuGe(2%) 400Å
382-2	Nb 280Å / CuGe(5%) 20Å
382-4	Nb 280Å / CuGe(5%) 40Å
382-8	Nb 280Å / CuGe(5%) 100Å
382-10	Nb 280Å / CuGe(5%) 200Å
389-9	Nb 280Å / CuGe(5%) 400Å
382-7	Nb 280Å / CuGe(5%) 700Å
344-10	Nb 280Å / CuMn(0.3%) 15Å
412-9	Nb 280Å / CuMn(0.3%) 20Å
344-9	Nb 280Å / CuMn(0.3%) 30Å
344-7	Nb 280Å / CuMn(0.3%) 60Å
344-6	Nb 280Å / CuMn(0.3%) 100Å
344-4	Nb 280Å / CuMn(0.3%) 400Å

Table 4 - Fitting parameters for all samples measured in the perpendicular orientation.

Sample Number	$H_{c2_0}^{\perp}$ (G)	$P_c^{\perp}$	$H_{irr_0}^{\perp}$ (G)	$P_{irr}^{\perp}$	$T_{c_0}^{\perp}$ (K)
456-16	24100±2800	1.00±0.06	25500± 1700	1.35±0.04	8.93±0.02
360-7	28400±5000	0.99±0.07	31100± 3400	1.27±0.06	8.25±0.02
360-9	25400±2600	1.00±0.05	39900± 3100	1.44±0.04	8.26±0.01
360-11	25000±1200	1.05±0.02	27500± 800	1.50±0.02	7.83±0.01
360-13	17300±1600	1.09±0.06	23700± 1800	1.70±0.05	7.37±0.02
440-7	13700±1100	1.14±0.06	16100± 1300	1.46±0.06	6.64±0.02
360-12	7400± 500	0.92±0.05	7100± 400	1.19±0.04	6.00±0.02
622-3	20800±3200	0.90±0.07	41300± 7800	1.48±0.08	8.39±0.02
622-4	31900±2600	1.13±0.04	29500± 2100	1.38±0.04	8.32±0.01
622-5	25100±3700	1.03±0.07	19900± 1900	1.23±0.05	8.17±0.02
622-6	22400±3000	0.99±0.07	35900± 3500	1.50±0.05	8.03±0.02
622-7	27100±6600	1.13±0.12	55400±10600	2.05±0.12	8.03±0.04
622-8	22600±2800	1.11±0.07	49600± 4900	1.93±0.07	7.83±0.02
622-9	20300±3100	1.07±0.08	24900± 2500	1.51±0.06	7.71±0.02
622-10	18500±1300	1.14±0.04	23700± 2100	1.57±0.05	7.41±0.02
622-11	16700±2400	1.08±0.08	21500± 2400	1.59±0.08	7.33±0.03
382-2	21600±3400	0.95±0.07	124000±24200	2.05±0.10	8.43±0.02
382-4	22300±3100	0.97±0.06	54600± 5900	1.80±0.06	8.27±0.02
382-8	19700±1900	0.96±0.05	63900± 5300	2.00±0.05	7.91±0.01
382-10	22600±3700	1.09±0.09	19100± 1200	1.69±0.05	7.47±0.03
389-9	15400±1700	0.98±0.06	27500± 2000	1.87±0.05	7.06±0.02
382-7	15300±2500	0.94±0.09	20400± 1800	1.80±0.07	6.89±0.03
344-10	29200±6100	1.06±0.08	56500±10200	1.66±0.08	7.93±0.01
412-9	22400±5700	0.93±0.12	88000±20200	2.01±0.13	7.73±0.03
344-9	25400±3200	1.08±0.06	63500± 6500	1.90±0.06	7.51±0.02
344-7	22900±5600	1.32±0.13	65300±15200	2.23±0.15	6.98±0.04
344-6	13200±1300	0.98±0.06	13300± 1400	1.42±0.07	6.10±0.02
344-4	4900±2000	0.86±0.17	11000± 3200	1.82±0.17	4.52±0.02

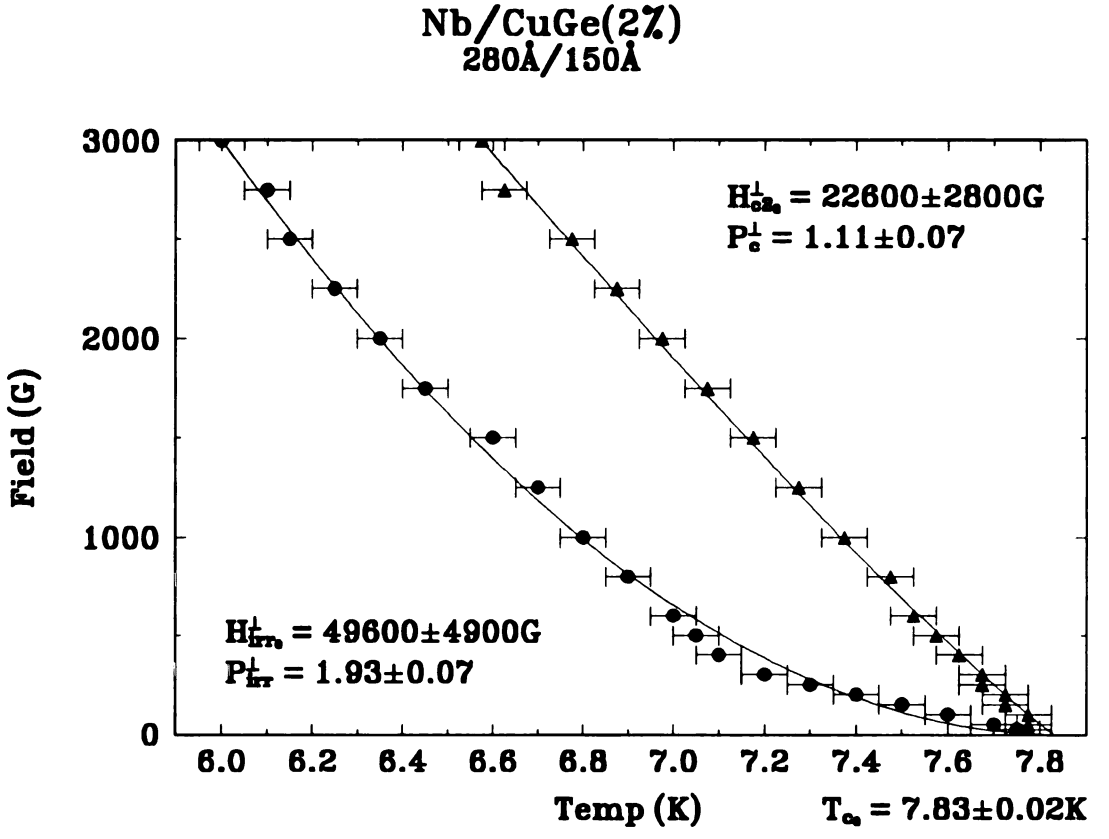

Figure 23 - The H T phase diagram for the Nb 280Å / CuGe(2%) 150Å sample.

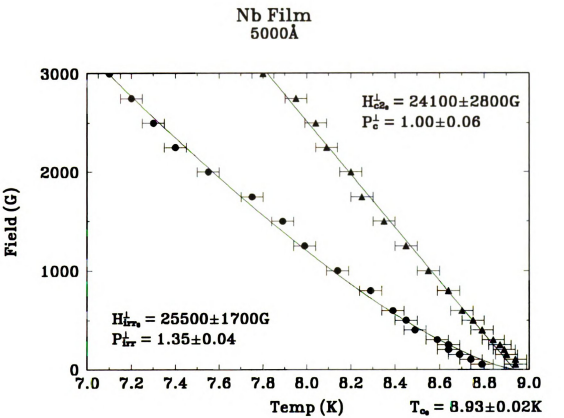

Figure 24 - The H T phase diagram for the 5000Å Nb film.

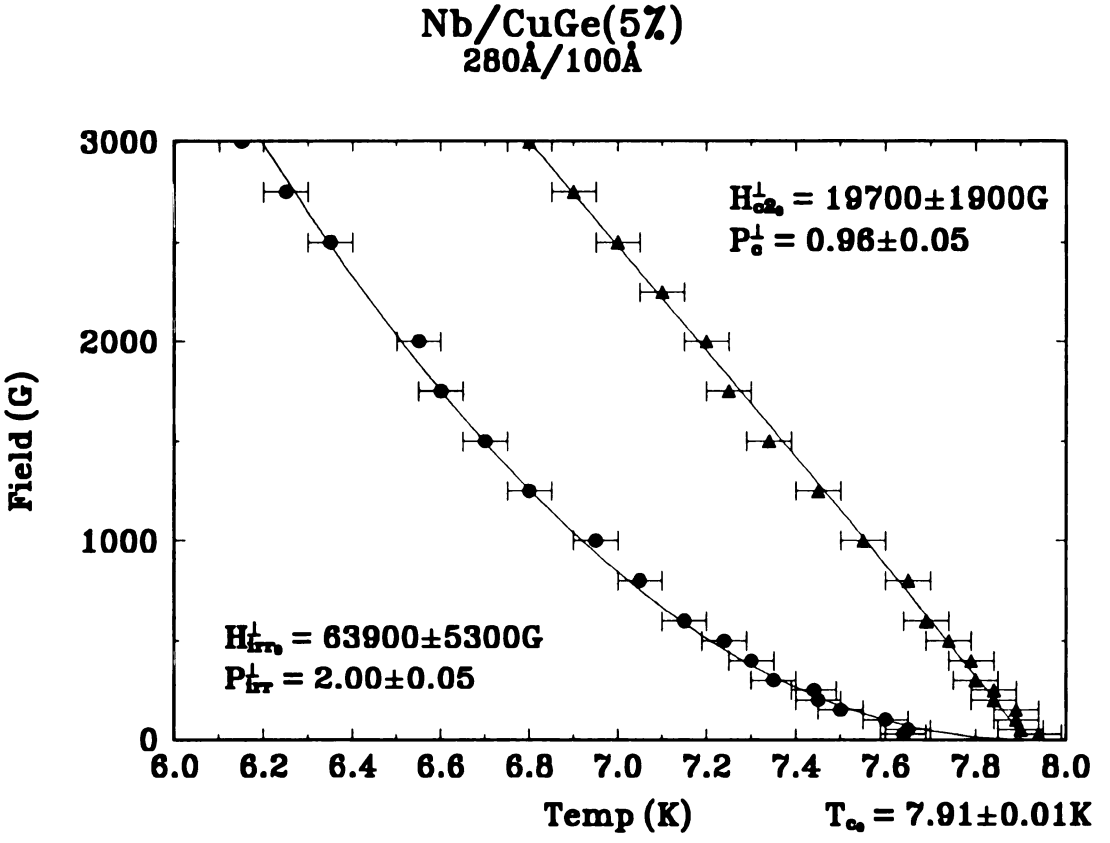

Figure 25 - The H T phase diagram for the Nb 280Å / CuGe(5%) 100Å sample.

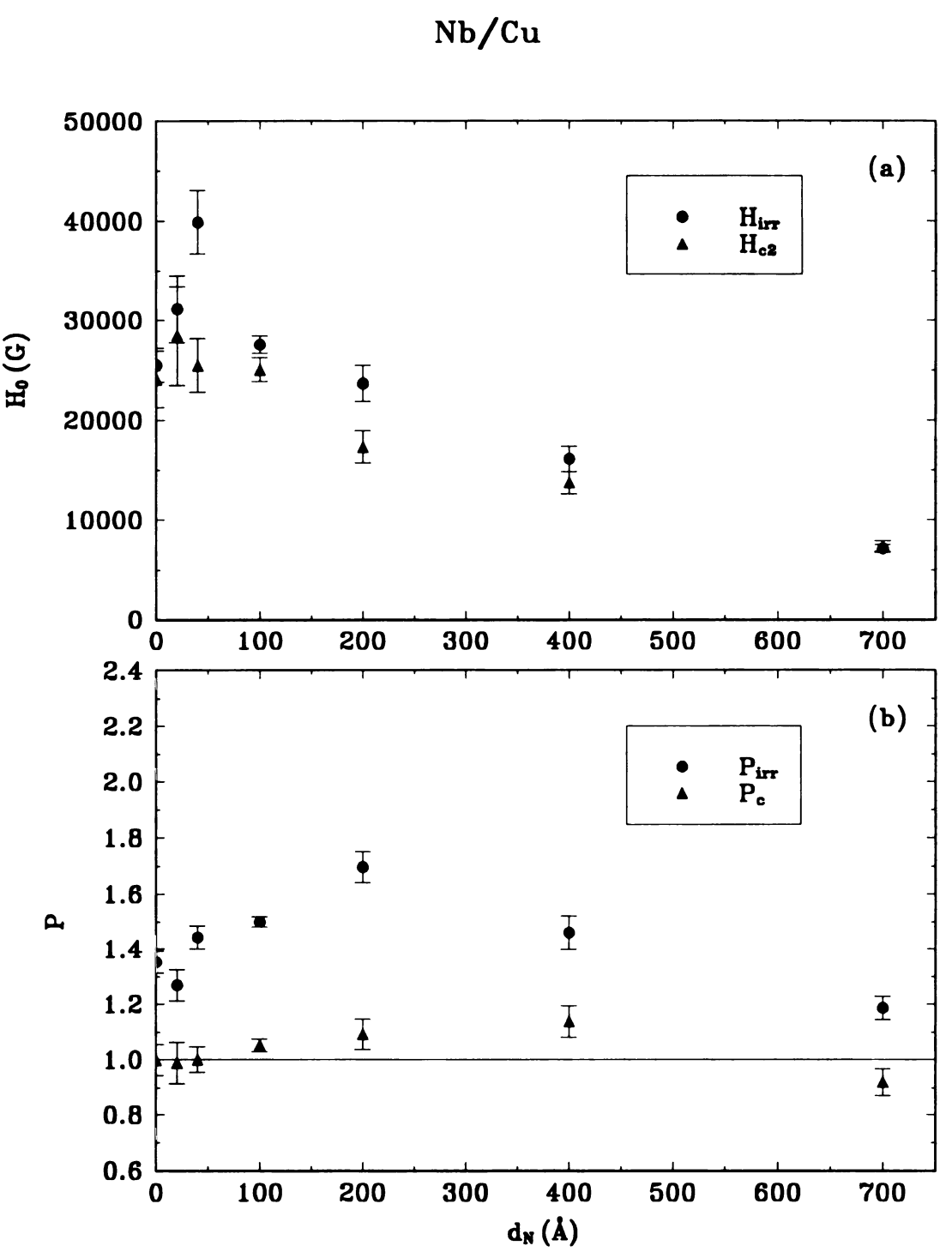

Figure 26 - H_{c2_0}, H_{irr_0}, P_c and P_{irr} versus d_N for the Nb/Cu samples.

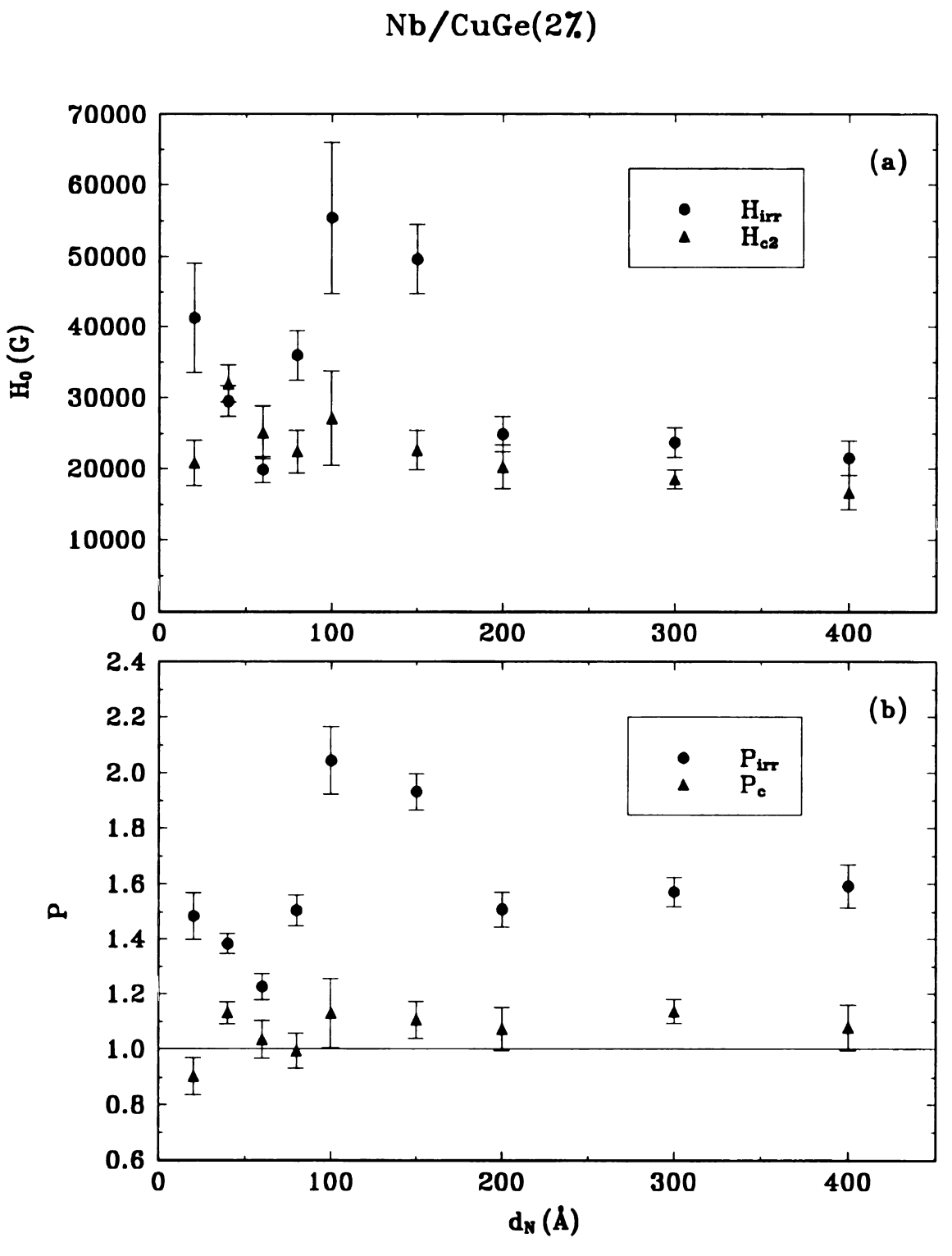

Figure 27 - H_{c2_0}, H_{irr_0}, P_c and P_{irr} versus d_N for the Nb/CuGe(2%) samples.

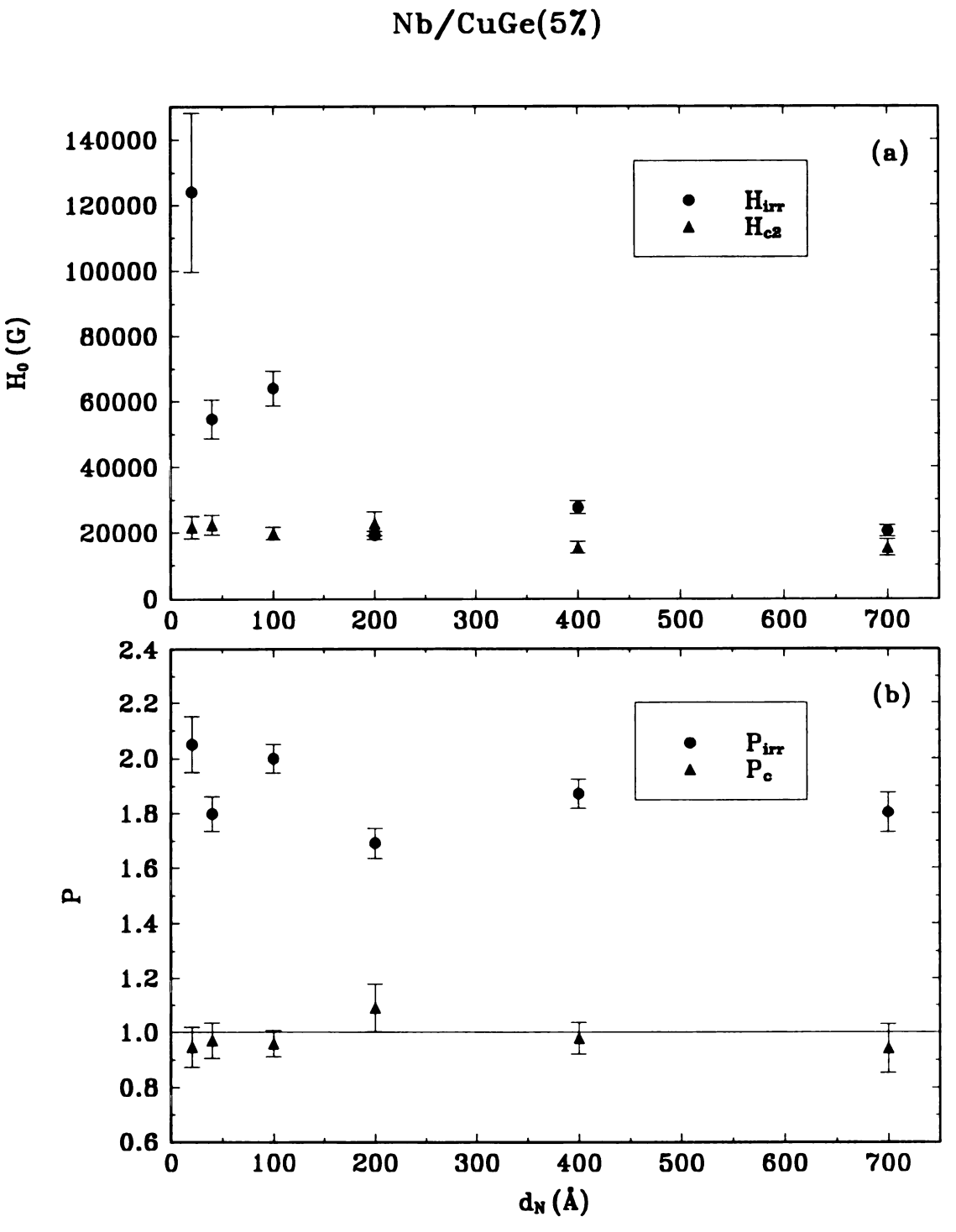

Figure 28 - H_{c2_0}, H_{irr_0}, P_c and P_{irr} versus d_N for the Nb/CuGe(5%) samples.

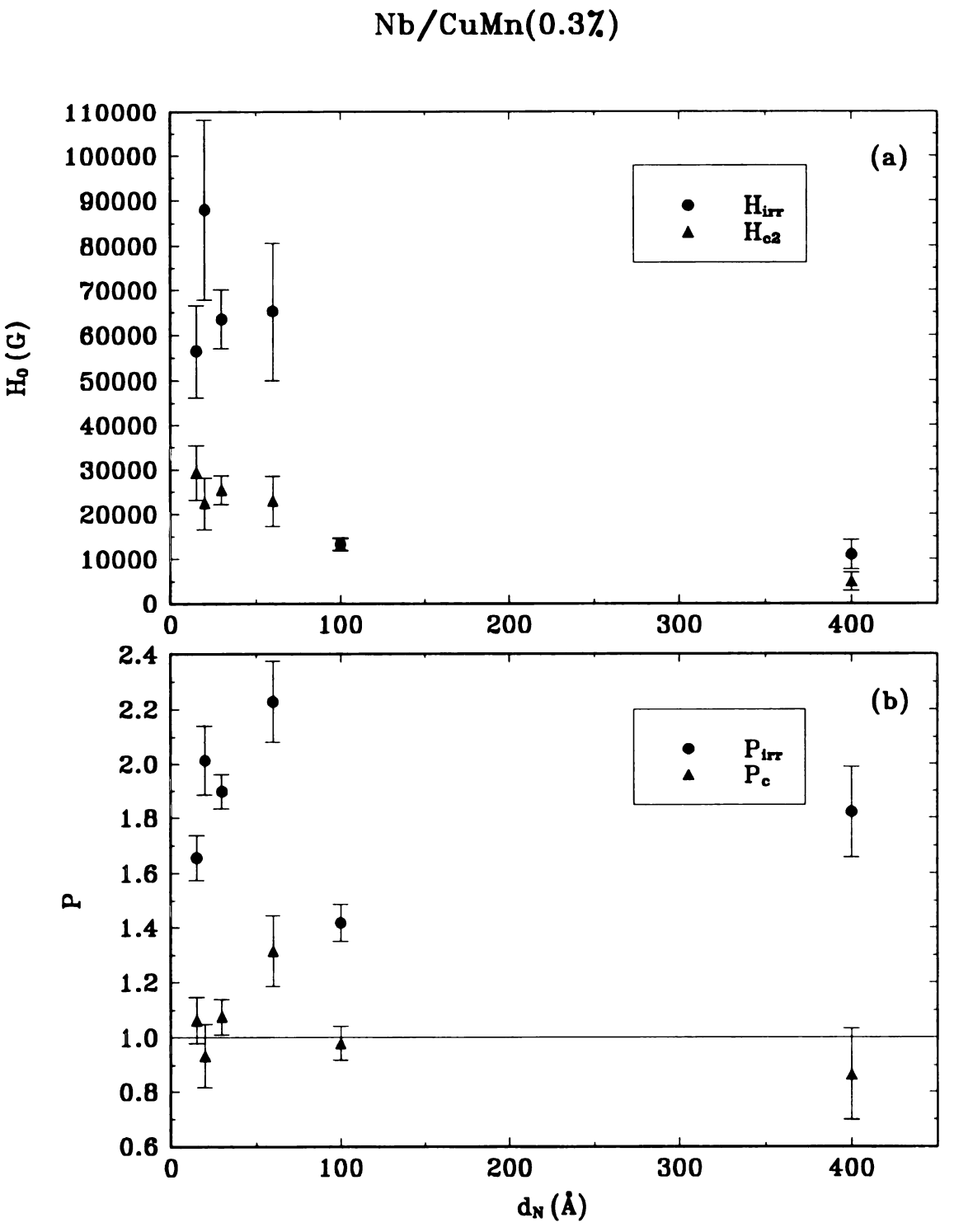

Figure 29 - H_{c2_0}, H_{irr_0}, P_c and P_{irr} versus d_N for the Nb/CuMn(0.3%) samples.

parameters for the Nb/CuGe(2%), the Nb/CuGe(5%), and the Nb/CuMn(0.3%) samples respectively.

H_{c2_0} and H_{irr_0} decrease with increasing normal metal layer thickness, due to the decrease of T_{c_0} with increasing d_N. Figure 30 illustrates this dependence of T_{c_0} on d_N for all sample types.

From these graphs one can conclude that P_c is a constant and equal to one within the noise of the data. This is the expected result for $H_{c2}(T)$. Although there is significantly more scatter in the P_{irr} data, it can be argued that for each interlayer type P_{irr} is a constant.

In an attempt to investigate the proposed 2D to 3D transition the Nb/CuGe(x%) parameters were also graphed as a function of Ge concentration. P_c, P_{irr}, and T_{c_0} are graphed as a function of Ge concentration for the Nb 280Å / CuGe(x%) 20Å samples in Figure 31. These samples should represent strongly proximity coupled S layers. For all samples P_c and T_{c_0} are constant but P_{irr} shows an interesting trend. P_{irr} is less then 1.5 for the 0% and 2% samples but jumps to over 2.0 for the 5% sample. This may indicate the formation of 2D pancake vortices in the Nb layers, the 3D line vortices being destroyed by the added impurities in the N layers. The impurities severely weaken the superconductivity in the N layers, thereby destroying the coupling between S layers. A similar graph for the Nb 280Å / CuGe(x%) 100Å samples, Figure 32, where the S layers are now moderately proximity coupled is consistent with this picture. Here the jump in P_{irr} is now occurring between 0% and 2%, it being easier to destroy the 3D line vortices in the thicker N layers. To test this hypothesis the 5% sample was irradiated at the

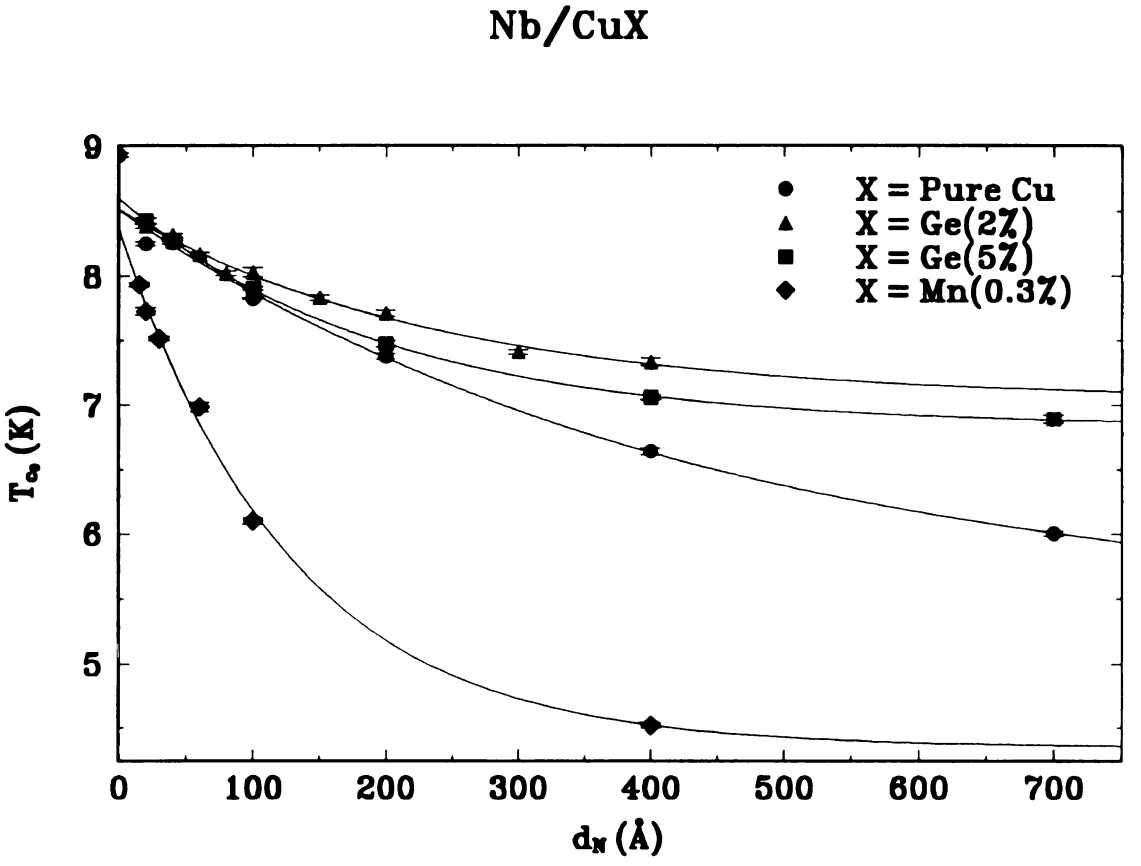

Figure 30 - T_{c_0} versus d_N for all sample types.

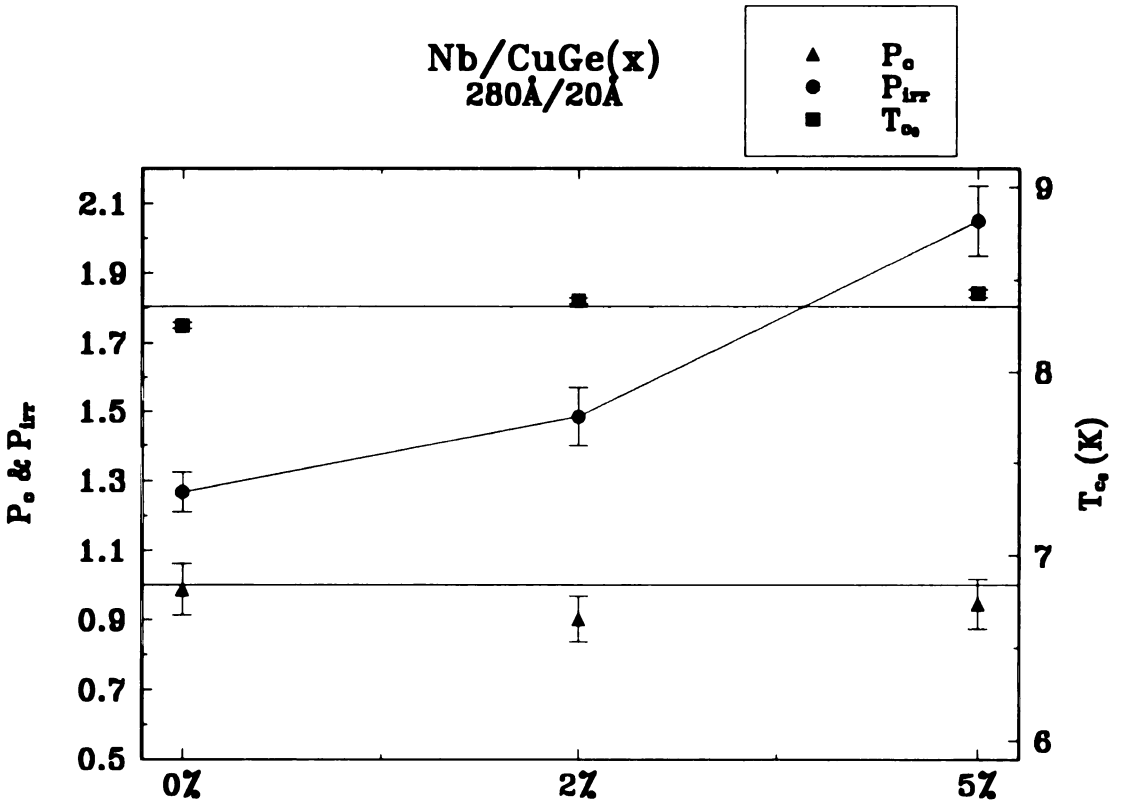

Figure 31 - P_c, P_{irr} and T_{c_0} graphed as a function of Ge concentration for the Nb 280Å / CuGe(x%) 20Å samples.

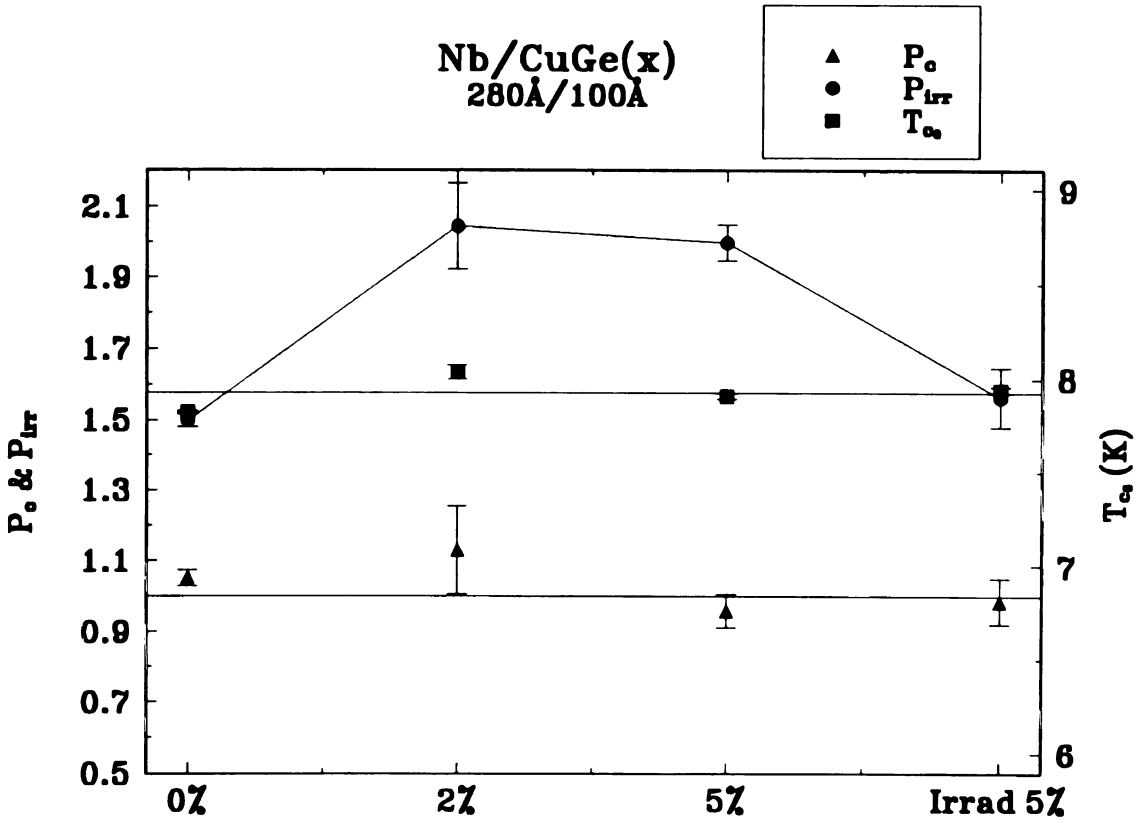

Figure 32 - P_c, P_{irr} and T_{c_0} graphed as a function of Ge concentration for the Nb 280Å / CuGe(x%) 100Å samples.

MSU-NSCL cyclotron to create columnar defects in the sample and see if the 3D line vortices could be restored. A total fluence of 5×10^{11} Kr^{+13} nuclei, each having an energy of 1.64 GeV, irradiated a sample area of about 0.25 cm^2. As seen in Figure 32, P_{irr} was indeed restored to a value close to 1.5.

One would expect that as d_N continued to increase the jump in P_{irr} from 1.5 to 2 would continue to occur at lower and lower concentrations. This appears not to be the case as can be seen in Figure 27. Here it is noted that although P_{irr} is near 2 for the two samples with d_N values of 100Å and 150Å, the samples with d_N values of 200Å, 300Å, and 400Å all have P_{irr} values near 1.5. However there are some concerns about the quality of the data collected for these three samples. The 200Å and 400Å samples showed uncharacteristic paramagnetic bumps in both the ZFC and FC magnetization curves just below T_c. Also the irreversibility between the ZFC and FC magnetization curves unexpectedly disappeared near 2500G for all three samples. This behavior was not seen in any of the other samples. Due to these concerns the P_{irr} values reported for these three samples may be misleading.

5.2.2 Parallel

All the Nb/Cu samples were measured in the parallel orientation. Figure 33 shows the H T phase diagram for the Nb 280Å / Cu 400Å sample. This was the only sample that showed a clear irreversibility in the FC and ZFC magnetization curves. For the other samples the data was just too noisy to extract meaningful T_{irr} values. Even this parallel

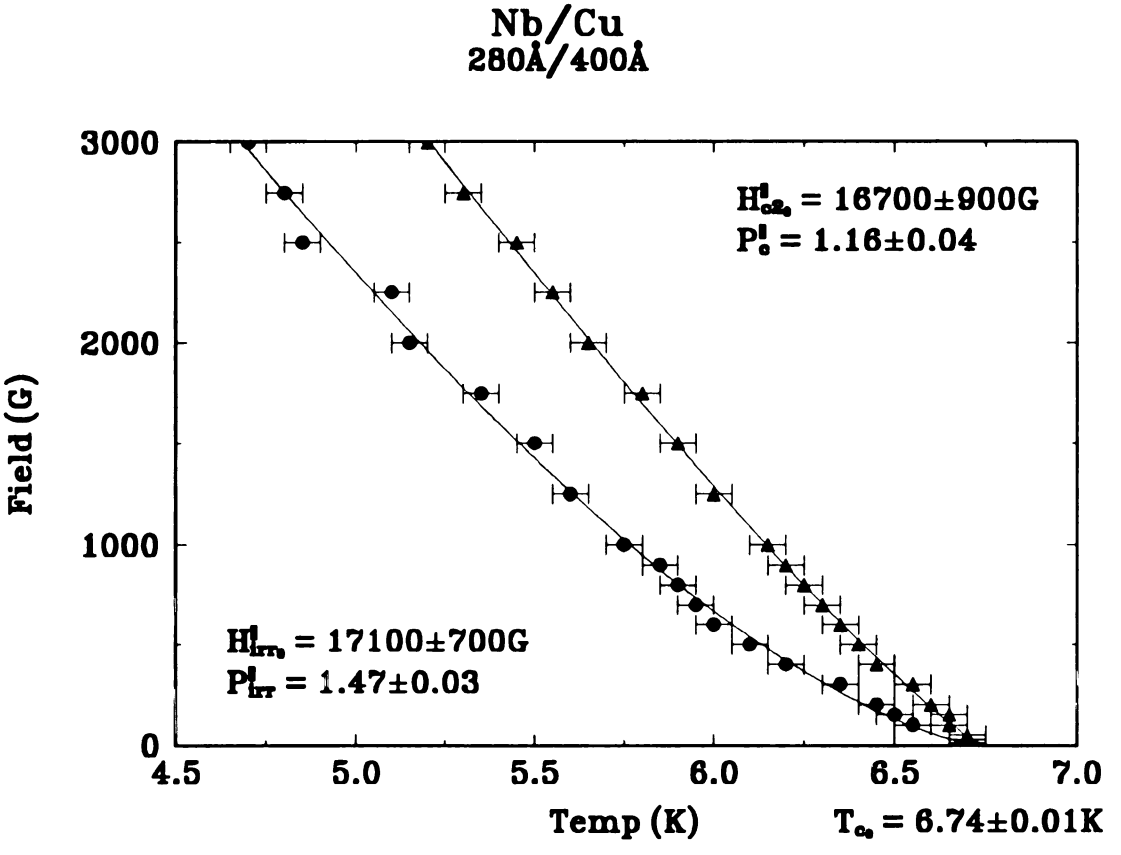

Figure 33 - The H T phase diagram for the Nb 280Å / Cu 400Å sample with the field applied parallel to the layers.

data proved to be difficult to reproduce because small misalignments produced very different results.

5.3 Conclusions

In the perpendicular orientation one sees an interesting trend in H_{irr_0} and H_{c2_0}. H_{irr_0} and H_{c2_0} decrease with increasing normal metal layer thickness which is expected due to the similar behavior of T_{c_0}. It is surprising however that H_{irr_0} and H_{c2_0} are essentially equal to each other in all samples as there are no theoretical predictions that this should be the case. The one case where this breaks down is for small d_N in the Nb/CuGe(5%) and Nb/CuMn(0.3%) samples. For $d_N \leq 100$Å in the Nb/CuMn(0.3%) samples and $d_N < 100$Å in the Nb/CuGe(5%) samples, H_{irr_0} is about a factor of 3 greater than H_{c2_0}. Since these are the two samples types where the coupling between S layers should be the weakest, this may be an indication of the 3D to 2D transition. The increase in H_{irr_0} is consistent with the increased pinning strength expected with the 3D line vortices, however since both H_{irr_0} and H_{c2_0} are extrapolated back to zero temperature from data taken at temperatures near T_{c_0}, the actual low temperature values of H_{irr} and H_{c2} are sure to be quite different than those found. This is evident form the fact that the actual irreversibility line can never cross $H_{c2}(T)$. Therefore the extrapolated values H_{irr_0} and H_{c2_0} are dependent on the temperature range over which data was taken, which

makes the comparison between different samples rather difficult. The corresponding values of P_{irr} and P_c are essentially constant for each sample type. P_c is roughly 1 for all samples as indicated by the solid line on the graphs, which is the expected value. P_{irr} is approximately 1.5 for the Nb/Cu and the Nb/CuGe(2%) samples which agrees with the value predicted by the flux creep model or the vortex glass model. P_{irr} is approximately 2 in the Nb/CuGe(5%) samples which agrees with the value predicted by the vortex lattice melting model. However considering the scatter present in the data, no firm conclusions can be drawn from these two observations. There is so much scatter in P_{irr} for the Nb/CuMn(0.3%) samples that it would be hard to pick between 2 and 1.5, but all values lie between 1.3 and 2.3. The strongest indication of the 3D/2D transition can be seen in the Nb/CuGe multilayers as a function of Ge concentration. The value of P_{irr} is 1.5 in a region where 3D line vortices are expected and the value jumps to 2 in a manner consistent with the picture of the formation of 2D pancake vortices.

In the parallel orientation, reproducible measurements could not be made with the available MPMS. The difficulty of measuring a consistent and reproducible irreversibility line in all orientations has been encountered by others[28], most of whom conclude that the study of transport properties has fewer inherent problems and is potentially more useful.

Chapter 6

CRITICAL CURRENT AND VORTEX PINNING

Critical current density and vortex pinning are two closely related properties of superconductors. The study of these properties has intensified recently due to the interest in making practical high-current applications of these materials. The fastest growing area of this type of research is the study of the highly anisotropic high-T_c ceramics, but many of the same physical processes take place in the low-T_c materials. With the greater control one has over the various parameters in low-T_c S/N multilayers (d_S, d_N, S, N, etc.) it should be easier to study these physical processes in the low-T_c materials and gain insight which should be transferable to the high-T_c superconductors. The critical current density, J_c, is defined as the current density at which an arbitrarily small voltage is observed. The vortex pinning force density, F_p, is equal to the critical value of the Lorentz force $\boldsymbol{J_c}\times\boldsymbol{B}$ per unit volume.

In this chapter, the theory of vortex pinning will be outlined. The results of critical current measurements on numerous Nb/CuX multilayers in two sample orientations will be shown. The agreement between theory and experiment will be discussed and conclusions presented.

6.1 Theory

The pinning of vortices in the vortex state by various imperfections in type-II superconductors is responsible for the existence of a critical current density, J_c, defined as the current density at which an arbitrarily small voltage is observed. The critical value of the Lorentz force per unit volume, F_p, is determined from J_c.

$$\mathbf{F}_p = \mathbf{J}_c \times \mathbf{B} \qquad \text{Equation [8]}$$

In the perpendicular orientation of an anisotropic superconductor there are two possible vortex states – 3D vortex lines and 2D vortex pancakes. As the vortex-vortex interaction within the layers overcomes the interaction between the layers, the 3D line vortices may break up into 2D pancakes. Severely reduced pinning results since pinning in one layer now has little or no effect on other layers.

Frietz and Webb[29] were the first to note that the pinning force density appeared to obey a scaling law of the form

$$F_p = \left[H_{c2}(T)\right]^{2.5} f(h), \qquad \text{Equation [9]}$$

where $f(h)$ is a function only of the reduced magnetic field $h = H/H_{c2}$. The importance of such a scaling law is that one could measure F_p at one temperature to get $f(h)$ and then simply scale the results by $\left[H_{c2}(T)\right]^{2.5}$ to predict F_p at any other temperatures. Though this first work was done on a number of Nb-based alloys, similar scaling laws of this form

$$F_p = \left[H_{c2}(T)\right]^{x} f(h), \qquad \text{Equation [10]}$$

have been shown to apply to a wide variety of other superconducting systems[30,31], with typical values of x being between 2 and 3.

The qualitative approach to understanding the features of $F_p(h,T)$ can be reproduced by a simple model presented by Kramer[30]. His model has the four following properties. First, at low reduced fields $F_p(h,T)$ is given by a function $F_1(h,T)$. Where F_1 is a pinning force computed on the assumption that all pinning interactions are broken, meaning that the maximum pinning forces have been exceeded upon reaching the critical Lorentz force. Second, at high reduced fields $F_p(h,T)$ is given by a function $F_2(h,T)$. Where F_2 is a pinning force computed on the assumption that strong pins do not break but rather the vortex state shears plastically around them. Third, the peak in $F_p(h,T)$ will be reached when $F_1(h,T) \approx F_2(h,T)$. Since F_2 is only weakly dependent on pinning strength, increasing the pinning strength and thus increasing F_1, will shift the peak in $F_p(h,T)$ to lower h and increase the peak value of $F_p(h,T)$, while leaving the high h values of $F_p(h,T)$ essentially unchanged. Fourth, the scaling law requires that both F_1 and F_2 depend on temperature as $H_{c2}^{x}(T)$.

A very interesting model that is still lacking a theoretical description is proposed by Koorevaar, Maj, Kes and Aarts[32]. The model they proposed was to explain the nonmonotonic behavior of J_c seen in Nb/NbZr multilayers as a function of field applied parallel to the multilayer. For their model they present the following simple phase diagram. For all $T < T_c$ a Meissner (M) phase exists at very low fields. In fields just above the Meissner phase there is an anisotropic Abrikosov (AA) region where the vortices are straight, as in an ordinary anisotropic superconductor. The modulation of the order

parameter is weak in this region. In fields above the AA region there is a kinked (K) region where the vortices now consist of disks with cores perpendicular to the layers and strings with cores along the layers, Figure 34. The field where a peak in J_c occurs, which they call H_p, is proposed to separate the AA and K regions. In the regime above H_p, J_c is determined from the motion of the disks along the layers and not the motion of the strings perpendicular to the layers as the intrinsic pinning related to the layered structure is too strong. Below H_p movement of the vortices normal to the layers is possible. One may expect that in the ideal case with the field applied parallel to the multilayers no vortices perpendicular to the planes (or disks) would be present. However, besides the fact that the sample can always have a small misalignment due to mounting, more important is the fact that the plane of the layers can vary in multilayers not grown epitaxially, making it impossible to align the sample exactly with the field.

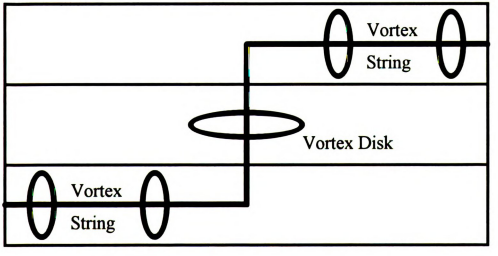

Figure 34 - An illustration of a kinked vortex region.

6.2 Experimental Results

For this study patterned samples had to be used as the large currents needed for the unpatterned samples produced heating in the contacts. Table 5 contains a list of all measured samples and their measurement orientation. Chapter 4 describes the actual procedures used to make the measurements. Once all the I-V curves for the various temperatures and fields are collected from the MPMS, the data is analyzed using a program that extracts all the critical currents. Also the $H_{c2}(T)$ curve is generated by extrapolating to the point where the critical current goes to zero. The $H_{c2}(T)$ curve is fit with the same functional form used in Chapter 5.

Table 5 - All samples measured in this study.

Sample Number	Sample Description	Measurement Orientation
707-2	3000Å Nb Film	⊥ and ||
782-1	280Å Nb Film	||
707-6	Nb 280Å / Cu 100Å	⊥ and ||
739-2	Nb 280Å / Cu 50Å	⊥ and ||
739-3	Nb 280Å / Cu 25Å	⊥
770-5	Nb 280Å / Cu 25Å	||
707-7	Nb 280Å / CuGe(2%) 100Å	⊥ and ||
770-6	Nb 280Å / CuGe(2%) 50Å	||
739-5	Nb 280Å / CuGe(2%) 25Å	⊥ and ||
723-5	Nb 280Å / CuGe(10%) 100Å	⊥
770-7	Nb 280Å / CuGe(10%) 100Å	||
770-8	Nb 280Å / CuGe(10%) 50Å	||
739-7	Nb 280Å / CuGe(10%) 25Å	⊥ and ||
707-8	Nb 280Å / CuMn(0.3%) 100Å	⊥ and ||
771-5	Nb 280Å / CuMn(0.3%) 50Å	||
771-6	Nb 280Å / CuMn(0.3%) 25Å	||

6.2.1 Perpendicular

In Figure 35 is shown a superposition of the I-V curves of the Nb/Cu 280Å/100Å sample collected at an applied field of 600G and a series of temperatures between 5 and 7K in 0.2K increments. As can be seen in the figure all the noise in the superconducting regime is below the 0.5 μV level. Therefore this value was chosen for the determination of I_c. Figure 36 shows the $H_{c2}(T)$ curve extracted for this sample and Figure 37 displays the critical current versus the reduced field h at various temperatures. The top curve is taken at 5K, the next curve at 5.2K, and so on in 0.2K increments. Note all curves are monotonically increasing with decreasing field with a sharp rise at low field where the sample enters the Meissner state. Figure 38 shows the pinning force density versus the reduced field h. Again the top curve is taken at 5K, the next curve at 5.2K, and so on in 0.2K increments.

If one compares the T_{c_0} of the patterned film shown in Figure 36 with that of a similar non-patterned film shown in Figure 22, it is noted that T_{c_0} of the patterned is significantly lower. This is true for all patterned films. This difference is probably due to the patterned film not being as clean as the non-patterned film because carbon impurities could be present in the patterned film due to the photoresist mask used during the sputtering process. Since carbon is atomic number 6, these impurities would not show up in the EDS analysis.

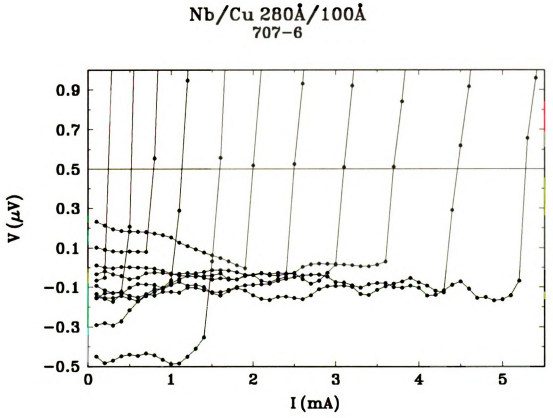

Figure 35 - Several of the I-V curves collected for the Nb/Cu 280Å/100Å sample. The right most curve is taken at 5K with each successive curve taken at higher temperatures in 0.2K increments.

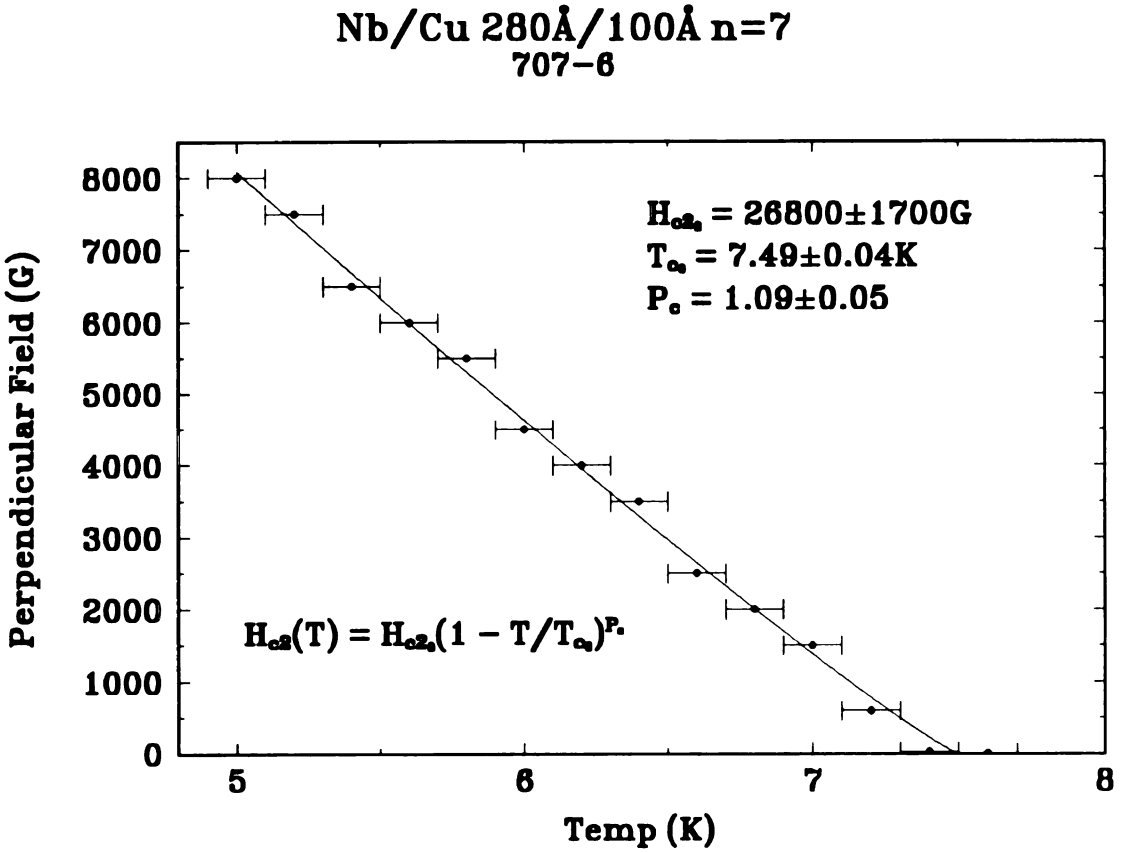

Figure 36 - The $H_{c2}(T)$ curve for the Nb/Cu 280Å/100Å sample.

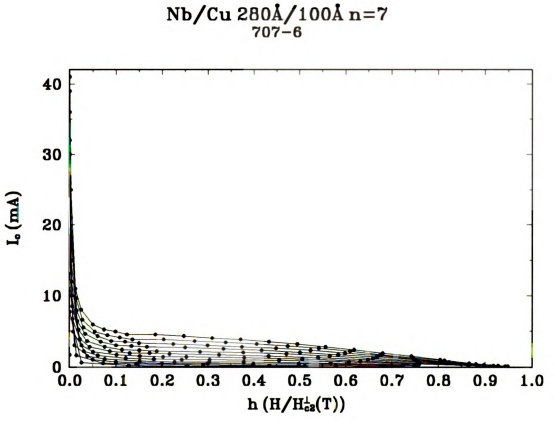

Figure 37 - The critical current versus reduced field *h* at various temperatures for the Nb/Cu 280Å/100Å sample.

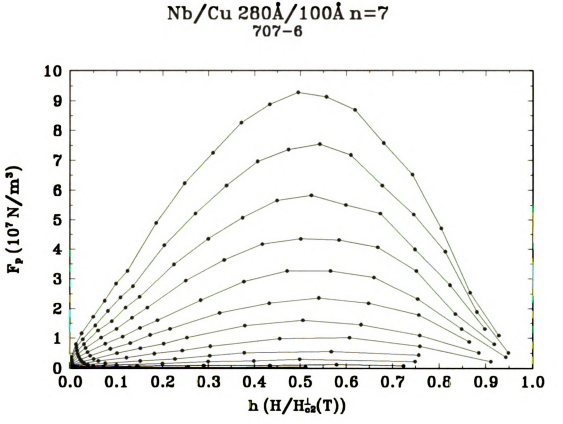

Figure 38 - The pinning force density versus reduced field *h* at various temperatures for the Nb/Cu 280Å/100Å sample.

As predicted, the pinning force data scales in agreement with the model presented by Kramer[30]. To check this, each F_p curve was fit with a function of the form:

$$F_p = prefactor\left[\left(\frac{m+n}{m}\right)h\right]^m\left[\left(\frac{m+n}{n}\right)(1-h)\right]^n \qquad \text{Equation [11]}$$

where m, n, and the *prefactor* are the fitting parameters. All curves were fit simultaneously with the same m and n values. This function was chosen arbitrarily as it had approximately the same shape as the data. It went to zero at $h = 0$ and 1 as needed and has a peak between $h = 0$ and 1. The only really important parameter in the above fit is the *prefactor*. The advantage of using this method to extract a scaling prefactor as opposed to extracting only the maximum of each F_p curve is the fact that the whole curve is being considered rather than just the peak value of the curve. Figure 39 is a graph of the scaled data for the Nb/Cu 280Å/100Å sample. The scaling prefactors were then fit to the form

$$prefactor = const\left(1-\frac{T}{T_{c_0}}\right)^{P'} \qquad \text{Equation [12]}$$

where *const* and P' were fitting parameters. T_{c_0} was fixed to the same value found in the determination of $H_{c2}(T)$. Figure 40 is a graph of the prefactors for this same sample. To determine the value of x in Equation [10] you need $H_{c2}(T) = H_{c2_0}\left(1 - T/T_{c_0}\right)^{P_c}$ along with the above equation. This produces the following relationship

$$x = \frac{P'}{P_c} \qquad \text{Equation [13].}$$

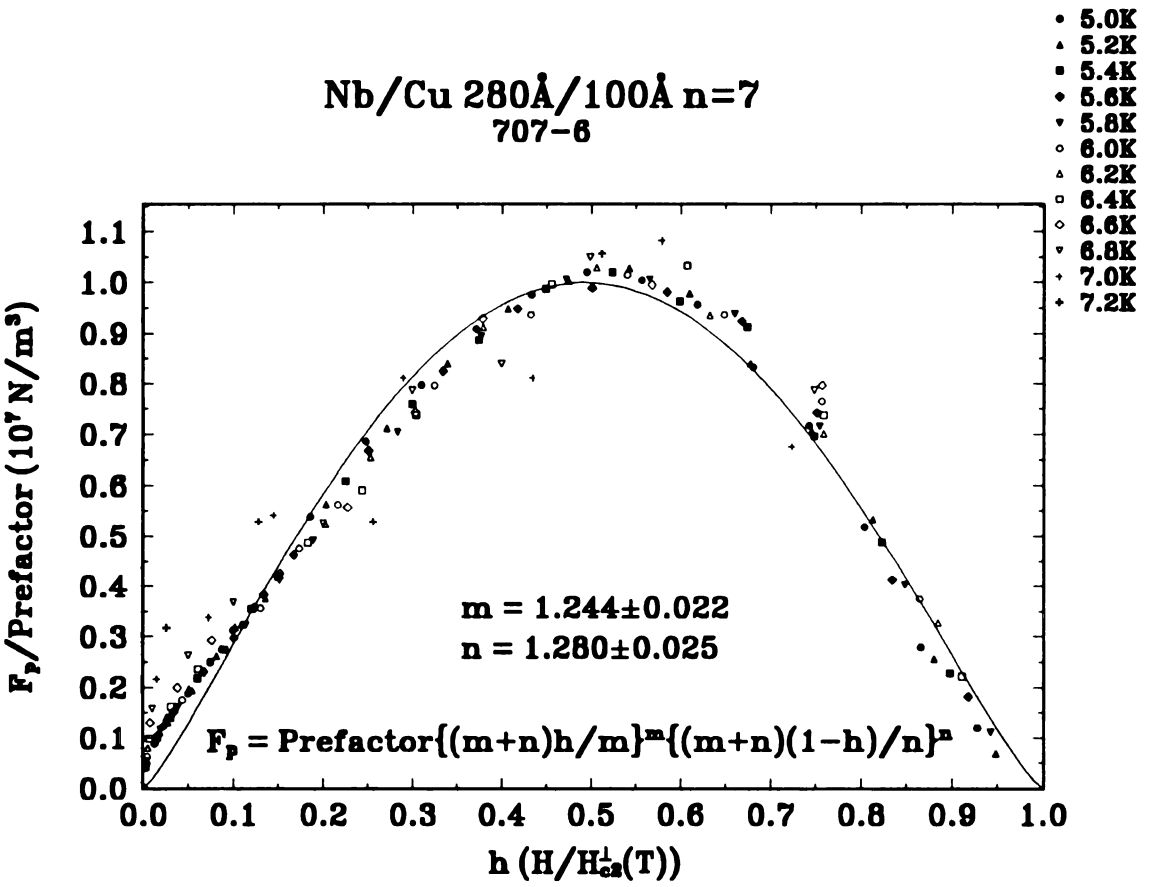

Figure 39 - Scaling of $F_p(h)$ for the Nb/Cu 280Å/100Å sample.

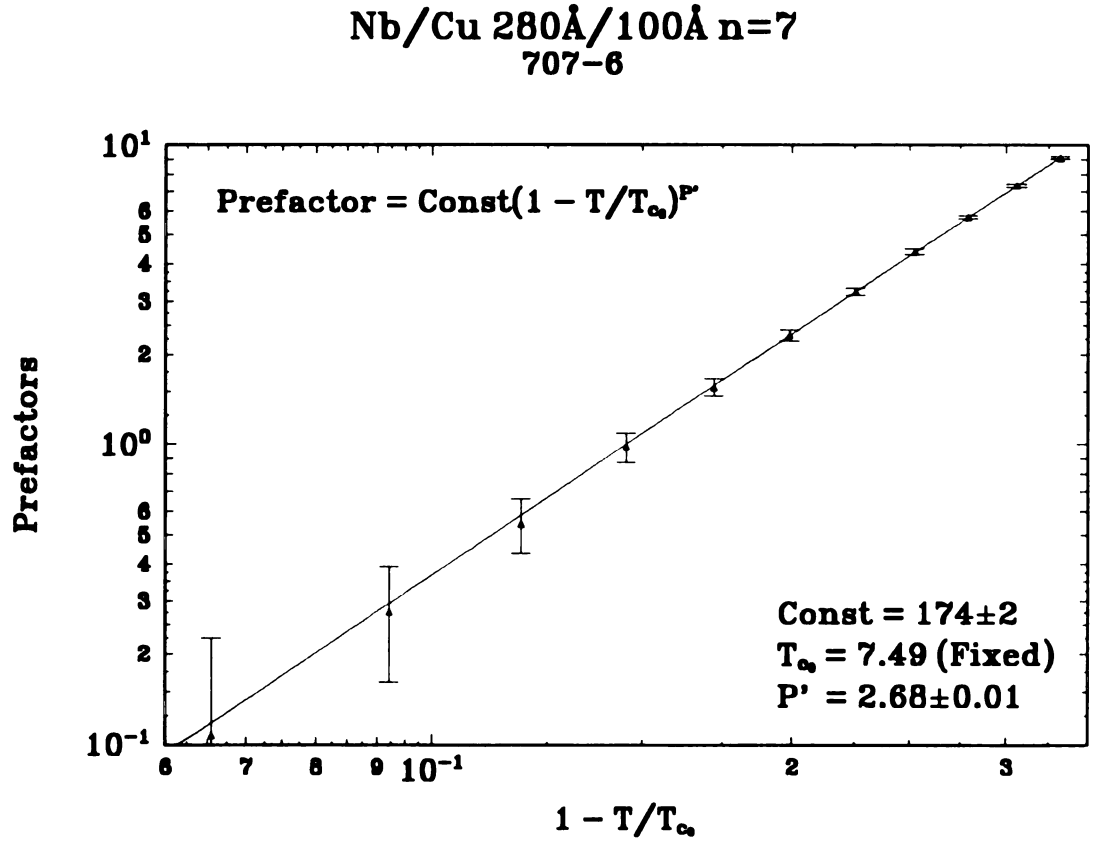

Figure 40 - Prefactors as a function of reduced temperature for the Nb/Cu 280Å/100Å sample.

All the samples measured with H perpendicular to the layers showed good scaling. Figures 41 and 42 illustrate the scaling of F_p for several other samples. Figure 43 is a graph of x versus d_N for all sample types. All multilayers have x values that fall in the expected range, between 2 and 3, with most clustered around 2.5.

The best evidence of the presence for a transition from 3D vortex lines to 2D vortex pancakes is seen when we graph F_p versus h for several samples of the same type at a fixed reduced temperature and compare them with what is seen in a thick (bulk) Nb film prepared in the same manner. Figures 44 and 45 are such graphs for the Nb/CuGe(2%) and Nb/CuGe(10%) samples respectively. In both figures it is seen that the $d_N = 25$Å samples have stronger pinning than in the bulk Nb sample where we know there are 3D line vortices. This makes sense if there are still 3D line vortices and the Ge serves as good pinning sites. However in the $d_N = 100$Å samples the pinning is greatly reduced indicating that the sample is now in the 2D vortex pancake state where the vortices in one layer are decoupled from the surrounding layers, meaning pinning in one layer has little to no effect in the other layers. Figure 46 is a similar graph for the Nb/Cu samples. Here we see a monotonic decrease of pinning strength with d_N. This could indicate that the 3D/2D crossover occurs at a d_N value less then 25Å or more likely that the pure Cu just doesn't serve as an effective pinner.

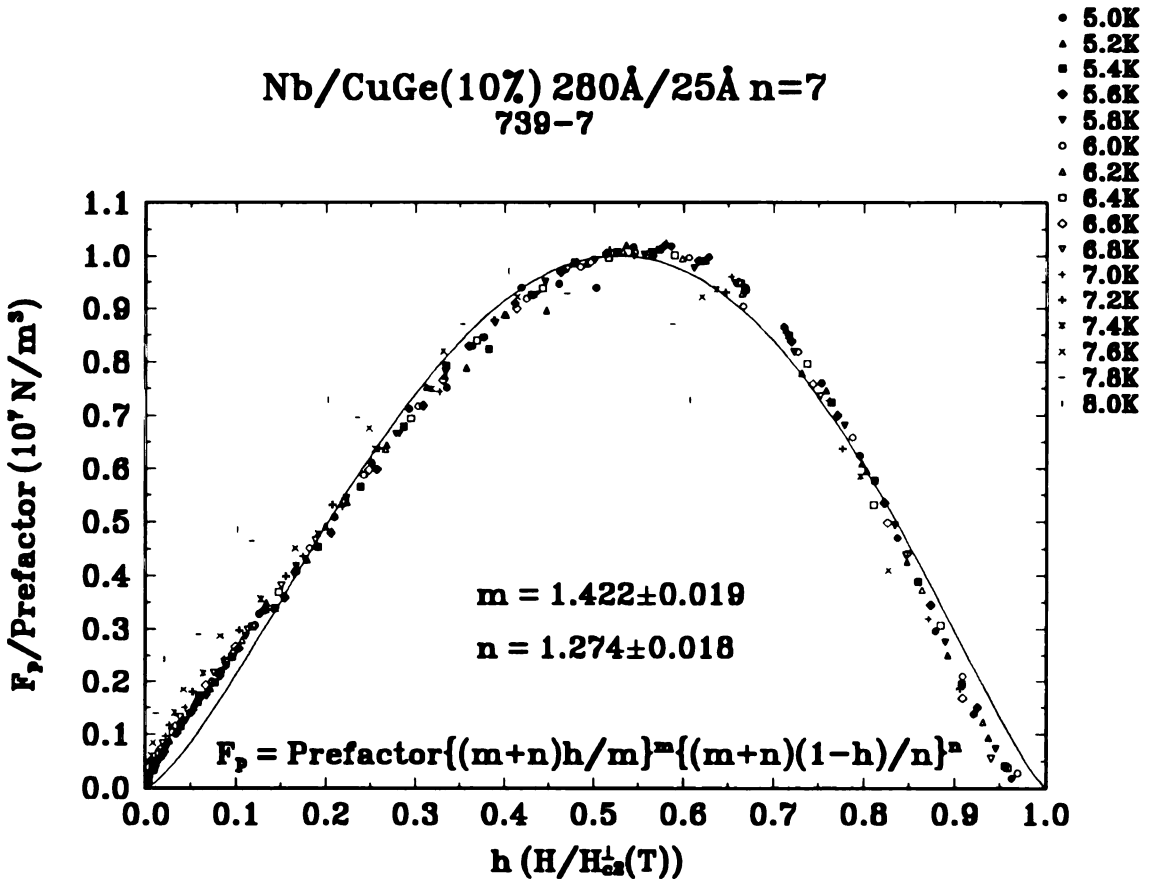

Figure 41 - Scaling of $F_p(h)$ for the Nb/CuGe(10%) 280Å/25Å sample.

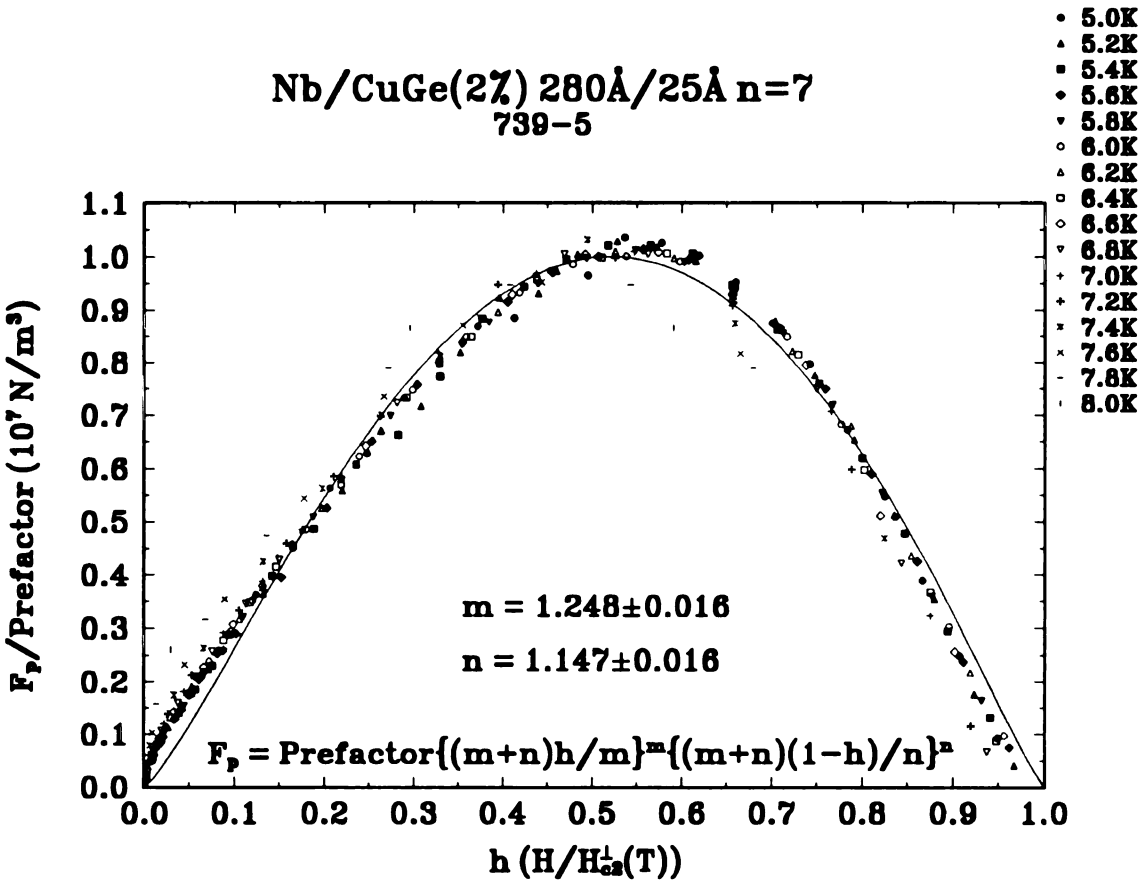

Figure 42 - Scaling of $F_p(h)$ for the Nb/CuGe(2%) 280Å/25Å sample.

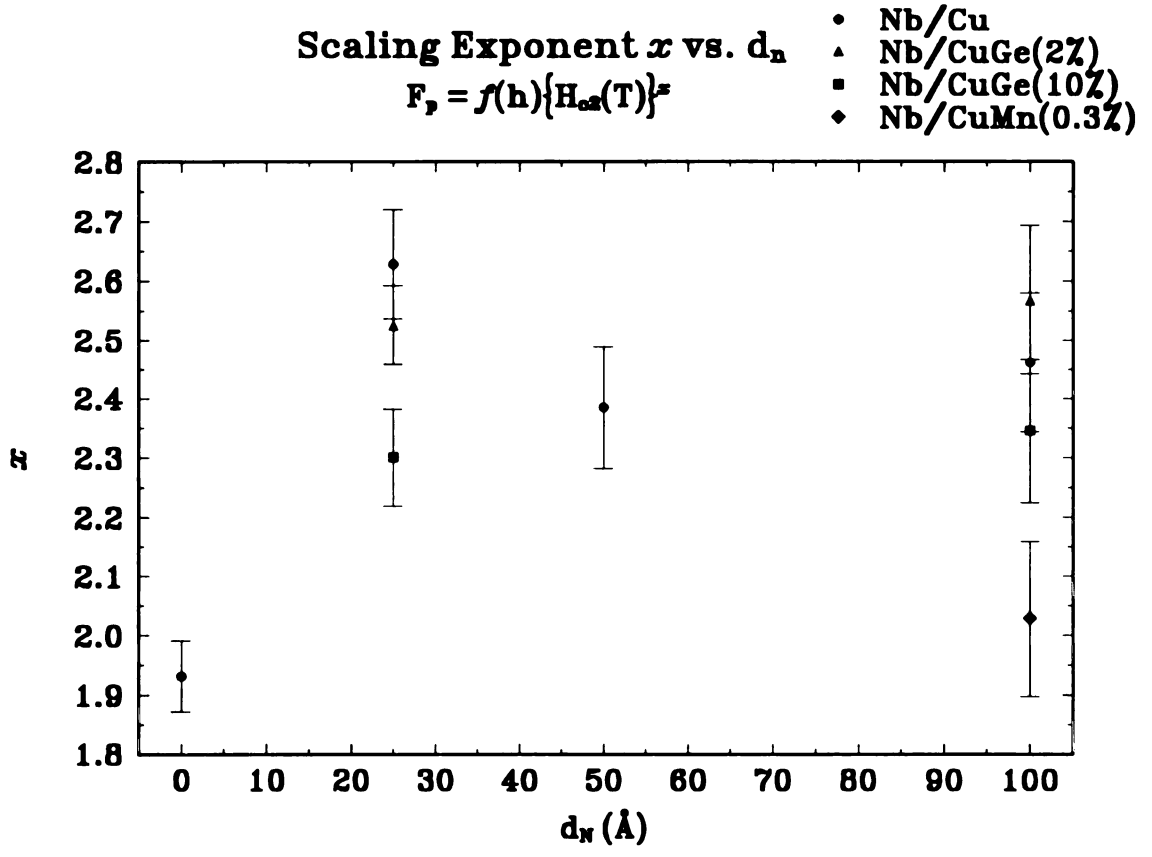

Figure 43 - A graph of x versus d_N for all sample types.

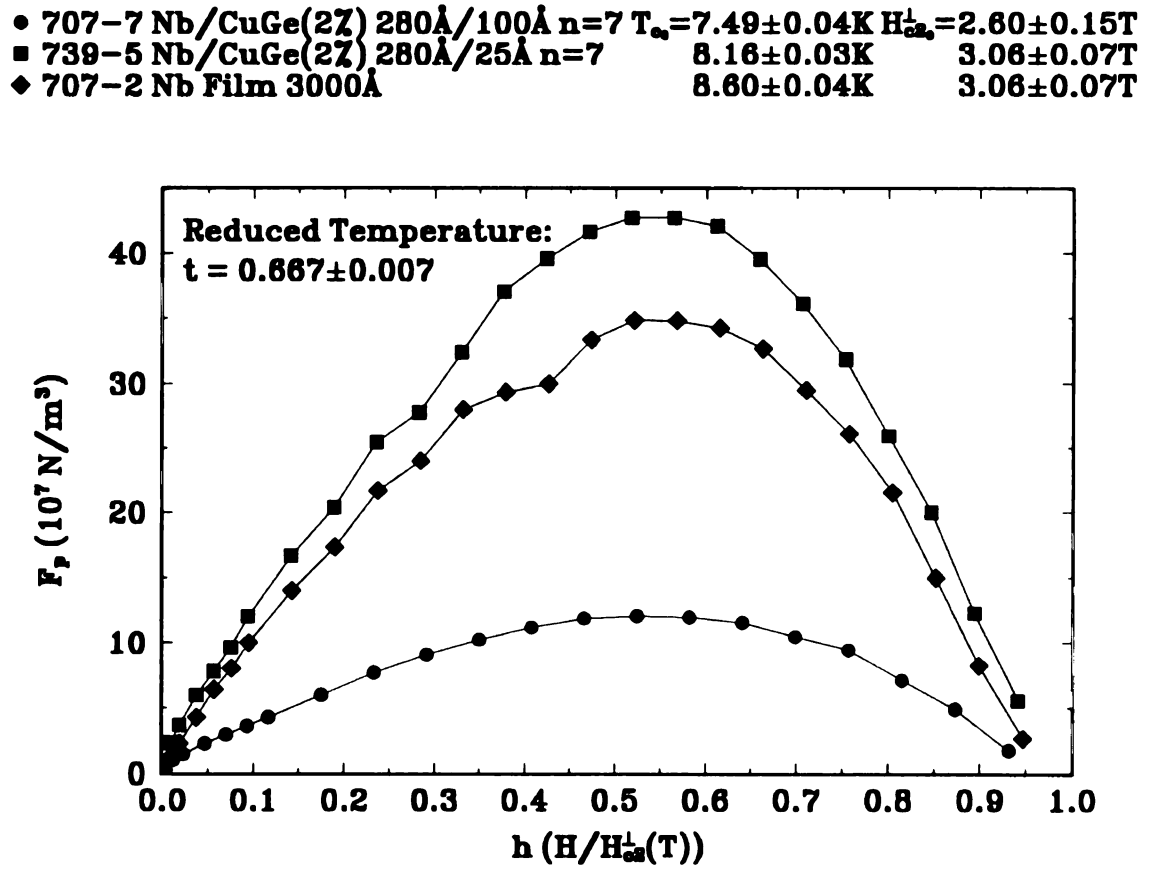

Figure 44 - F_p versus h at fixed reduced temperature for the Nb/CuGe(2%) samples.

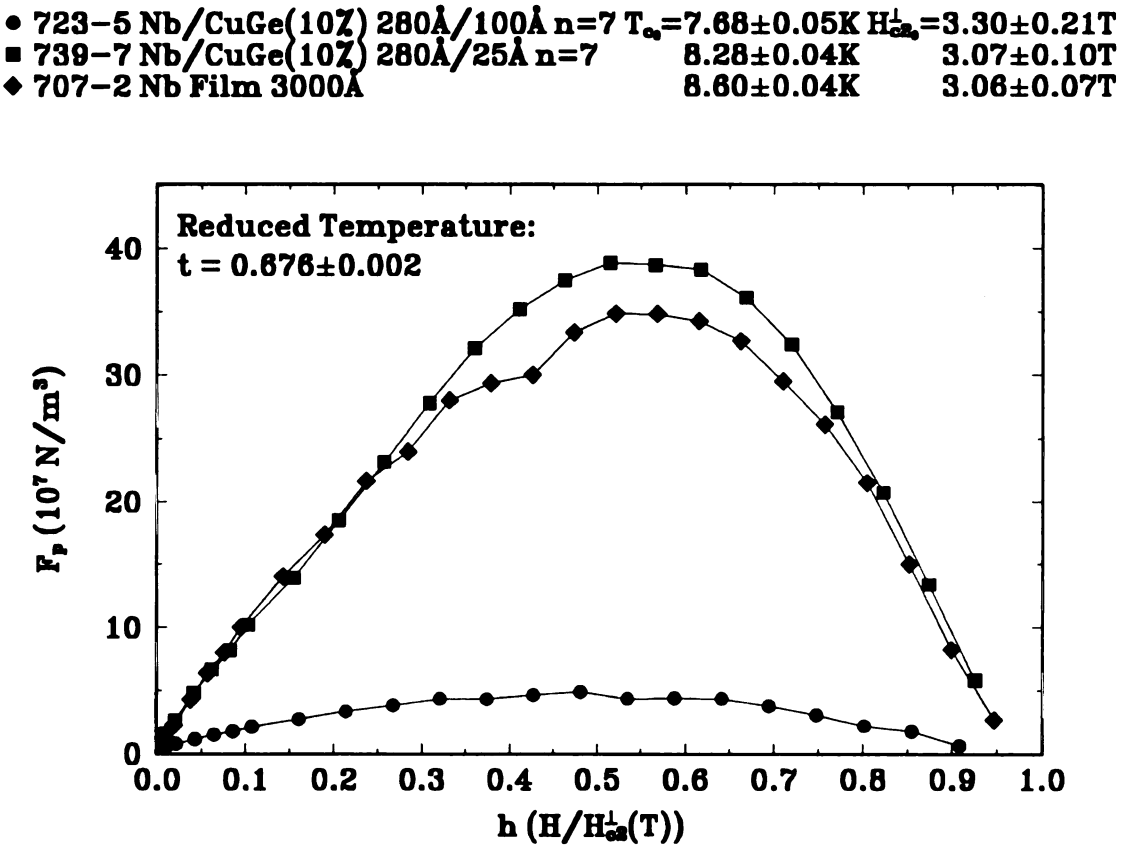

Figure 45 - F_p versus h at fixed reduced temperature for the Nb/CuGe(10%) samples.

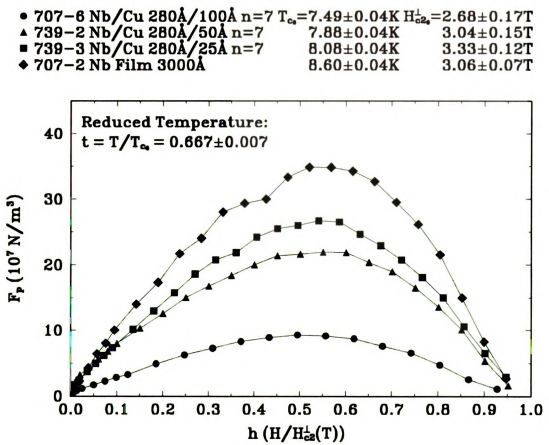

Figure 46 - F_p versus h at fixed reduced temperature for the Nb/Cu samples.

6.2.2 Parallel

Here the exact same procedure was used for extracting the critical currents and the $H_{c2}(T)$ curve as in the perpendicular case. However here the scaling fails. Figures 47 and 48 illustrate the best attempt at scaling on two of the parallel samples. However if one looks at the critical current, Figure 49, behavior similar to that described by Koorevaar, Maj, Kes, and Aarts[32] is seen. However instead of seeing a peak in I_c, more of a plateau is seen. This seems to indicate the structural vortex lattice transition they proposed is also present in our Nb/CuX samples. This may also account for why the data doesn't scale. Figure 49 and 50 are two I_c versus h diagrams. Again the top curve is taken at 5K, the next curve at 5.2K, and so on in 0.2K increments. Figure 50 includes two runs at 5K, the solid and open symbols, showing the reproducibility of the data. As in the perpendicular case a sharp rise is seen at low h as the sample enters the Meissner state.

However a more interesting property is seen in the pinning force density as a function of Ge concentration. Here the effects which reduce coupling between S layers and produce weak pinning in the perpendicular orientation, cause the N layers and their interfaces to be good pinning sites. This is exactly what is seen in Figure 51 where F_p is plotted versus h for two multilayers at three different temperatures. In the Nb/CuGe(2%) sample, pinning is comparable to that of a Nb film. In the Nb/CuGe(10%) sample, the pinning has increased by an order of magnitude and there is even a slight enhancement of T_{c_0}. The peak has shifted to a much lower value of h, which is explained by the model of flux pinning presented by Kramer[30].

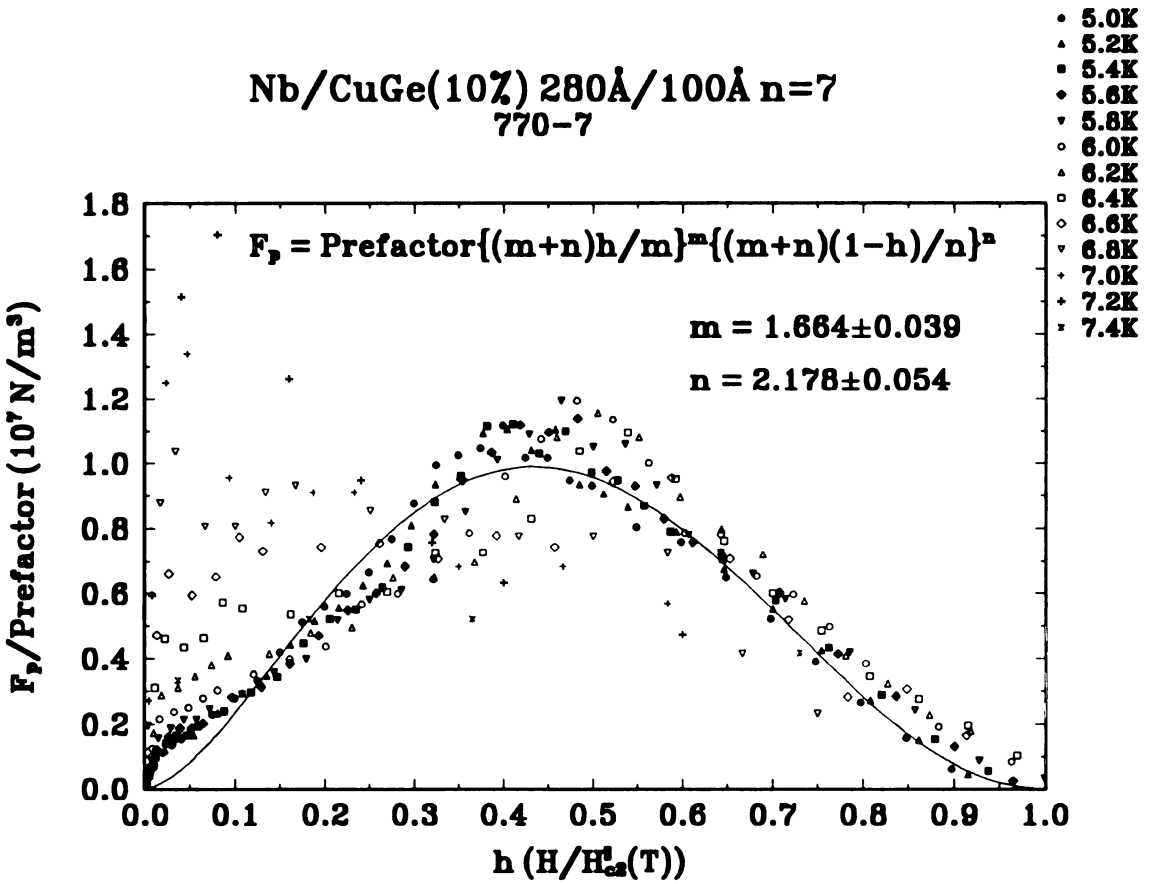

Figure 47 - Attempt at scaling F_p versus $h^{\parallel}$ for the Nb/CuGe(10%) 280Å/100Å sample.

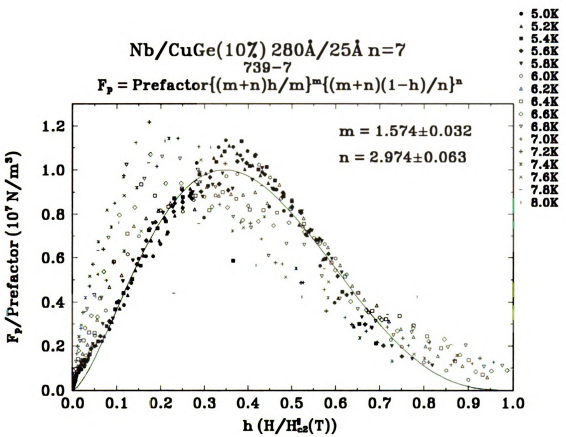

Figure 48 - Attempt at scaling F_p versus $h^{\dagger}$ for the Nb/CuGe(10%) 280Å/25Å sample.

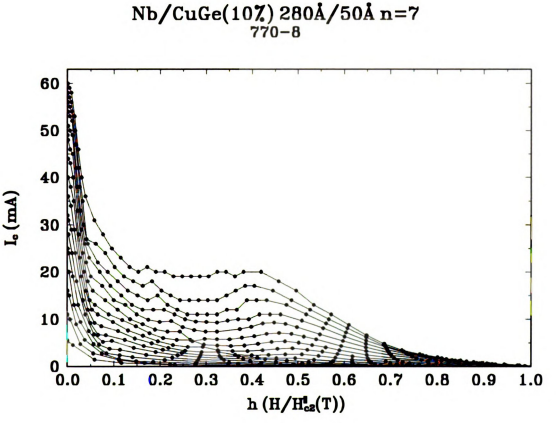

Figure 49 - The critical current versus reduced field $h^{\parallel}$ at various temperatures for the Nb/CuGe(10%) 280Å/50Å sample.

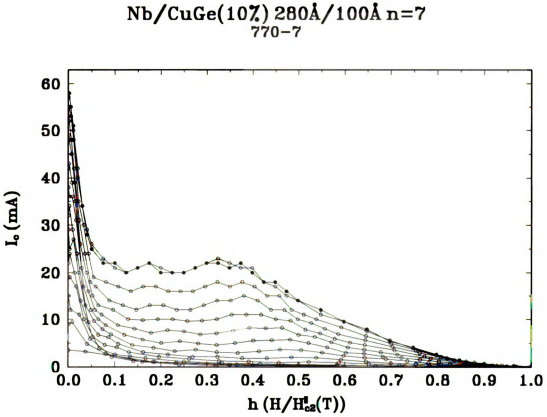

Figure 50 - The critical current versus reduced field $h^{\parallel}$ at various temperatures for the Nb/CuGe(10%) 280Å/100Å sample.

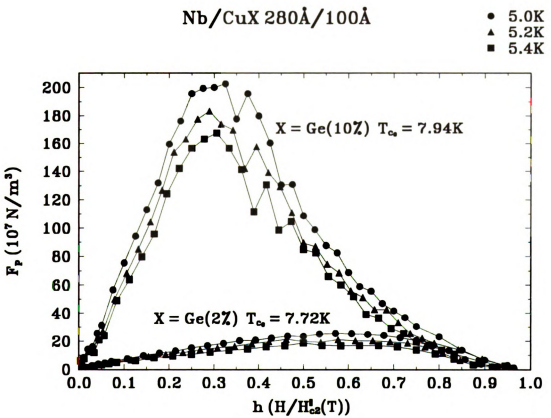

Figure 51 - F_P versus h at three different temperatures for the Nb/CuGe(2%) and Nb/CuGe(10%) 280Å/100Å samples.

6.3 Conclusions

In the perpendicular orientation F_p scales and the expected scaling exponent is found. There is also strong evidence for a transition from 3D vortex lines to 2D vortex pancakes as a function of normal metal layer thickness found in the Nb/CuGe(2%) and the Nb/CuGe(10%) multilayers. In both samples this transition occurs between 25Å and 100Å. For the Nb/Cu multilayers this same analysis proves inconclusive, possibly due to the lack of strong pinning sites in the pure Cu.

In the parallel orientation F_p does not scale, but there does appear to be evidence for a structural vortex lattice transition from a anisotropic Abrikosov region to a kinked region where the critical current density is now determined by vortex disks with their cores perpendicular to the layers. Since J_c is determined by two vastly different physical mechanisms in these two regions, it is not too surprising that F_p does not scale. It has also been demonstrated that the pinning strength of the N layers is affected by the addition of Ge, with no detrimental effects on T_c. In going from N layers of CuGe(2%) to CuGe(10%), the pinning strength increases by an order of magnitude.

Chapter 7

FUTURE DIRECTIONS

There is still a lot of theoretical work that needs to be done on the irreversibility line problem. The transition at T_{irr} is believed to be highly sensitive to disorder, being either first order or continuous depending on the number and geometry of impurities. There are however no theoretical predictions for how the nature of the impurities should affect the shape of the irreversibility line. There are also no theoretical predictions for how the 3D line / 2D pancake vortex transition should affect the shape of the irreversibility line. There are also several interesting properties that may be seen in the parallel orientation, like the 3D/2D/3D transition discussed earlier, which may influence the shape of the irreversibility line, but again there are no theoretical predictions. This is not to say that there is no direction for the experimental work to take. The use of a SQUID magnetometer which allows for the direction of the applied field to be aligned with the sample should greatly improve the reproducibility of the parallel measurements of the irreversibility line.

Due to the inherent difficulty in obtaining good and reproducible measurements of the irreversibility line with magnetization measurements, most future work will probably be directed toward the study of transport properties. The next step in the vortex pinning problem has already begun. Dr. P. Duxbury and his student Z. Zhou have begun a

detailed study into the vortex pinning energy present in layered superconductors. They started from Ginzburg-Landau theory and are using a six parameter model. Their model has two layer types and each is characterized by a coherence length, a penetration depth, and a thickness. They have started by doing some numerical calculations of the energy of a single vortex parallel to the layers as a function of displacement. Comparing the change in energy from one layer to the next allows one to calculate the pinning energy. They plan to add additional vortices to their model to take into the account the vortex-vortex interactions. They will also investigate the perpendicular orientation by looking at vortices perpendicular to the layers.

LIST OF REFERENCES

LIST OF REFERENCES

[1] G. Blatter, M. V. Feigel'man, V. B. Geshkenbein, A. I. Larkin and V. M. Vinokur, Rev. Mod. Phys. **66**, 1125 (1994).

[2] J. M. Slaughter, W. P. Pratt, Jr., and P. A. Schroeder, Rev. Sci. Instrum. **60** (1), 127 (1989).

[3] Si wafers were purchased from Silicon Quest International, 2904 Scott Blvd., Santa Clara, CA 95054.

[4] MICRO is a liquid laboratory cleaner purchased from International Products Corporation, P. O. Box 70, Burlington, NJ 08016.

[5] Kodak's part number is 1208966.

[6] Photoresist and developer were purchased from Shipley, 455 Forest Street, Marlborough, MA 01752.

[7] Plasma Therm Inc., 9509 International Ct, St. Petersburg, FL 33716.

[8] Angstrom Sciences, P. O. Box 18116, Pittsburgh, PA 15236.

[9] Aesar/ Johnson Matthey Inc., P. O. Box 8247, Ward Hill, MA 01835-0747.

[10] M. L. Wilson, Ph. D. dissertation, Michigan State University (1994).

[11] Quantum Design, 11578 Sorrento Valley Road, Suite 30, San Diego, CA 92121.

[12] Keithley, 28775 Aurora Road, Cleveland, OH 44139.

[13] M. Suenaga, D. O. Welch, and R. Budhani, Supercond. Sci. Technol. **5** S1 (1992).

[14] Matthew. F. Schmidt, N. E. Israeloff, and A. M. Goldman, Phys. Rev. B. 48, 3404 (1993).

[15] Purchased from Wilmad Glass Company, Inc., Route 40 & Oak Road, Buena, NJ 08310.

[16] Purchased from Electrical Insulation Suppliers, Inc., 19769 15 Mile Road, Mt. Clemens, MI 48043.

[17] Purchased from Apiezon Products, M&I Materials Ltd., P.O. Box 136, Manchester M60 1AN, England.

[18] Y. Yeshurun and A. P. Malozemoff, Phys. Rev. Lett. **60**, 2202 (1988).

[19] P. de Rango, B. Giordanengo, R. Tournier, A. Sulpice, J. Chaussy, G. Deutscher, J. L. Genicon, P. Lejay, R. Retoux and B. Raveau, J. Phys. France **50**, 2857 (1989).

[20] Z. J. Huang, Y. Y. Xue, R. L. Meng and C. W. Chu, Phys. Rev. B **49**, 4218 (1994).

[21] J. R. L. de Almeida and D. J. Thouless, J. Phys. A: Math Gen. **11**, 983 (1978).

[22] A. Houghton, R. A. Pelcovits and A. Subdø, Phys. Rev. B **40**, 6763 (1988).

[23] Y. M. Wan, S. E. Hebboul and J. C. Garland, Phys. Rev. Lett. **72**, 3867 (1994).

[24] Robert A. Hein, Thomas L. Francavilla and Donald H. Leibenberg, ed., *Magnetic Susceptibility of Superconductors and Other Spin Systems*, Plenum Press (1991).

[25] Youwen Xu and M. Suenaga, Phys. Rev. B **43**, 5516 (1991).

[26] J. H. P. M. Emmen, G. M. Stollman and W. J. M. De Jonge, Physicia C **169**, 418 (1990).

[27] L. Civale, T. K. Worthington and A. Gupta, Phys. Rev. B **43**, 5425 (1991).

[28] M. C. Frischherz, F. M. Sauerzopf, H. W. Weber, M. Murakami and G. A. Emel'chenko, Supercond. Sci. Technol. **8**, 485 (1995).

[29] W. A. Fietz and W. W. Webb, Phys. Rev. **178**, 657 (1969).

[30] Edward J. Kramer, J. Appl. Phy. **44** 1360 (1973).

[31] A. M. Campbell and J. E. Evetts, Adv. Phys. **21**, 372 (1972).

[32] P. Koorevaar, W. Maj, P. H. Kes, and J. Aarts, Phys. Rev. B **47**, 934 (1993).